ACTA TECHNICA JAURINENSIS
Vol. 15, No. 4, pp. 188-192, 2022
10.14513/actatechjaur.00669

Applications of periodic structures and metamaterials for antenna design

Péter Prukner[1,*], Miklós Kuczmann[2]

[1] Digital Development Center, Széchenyi Istvan University
Egyetem tér 1, 9026 Győr, Hungary
[2] Department of Automation, Széchenyi Istvan University
Egyetem tér 1, 9026 Győr, Hungary
*e-mail: peter.prukner@ddc.sze.hu

Submitted: 01/07/2022 Accepted: 06/08/2022 Published online: 31/08/2022

Abstract: Nowadays, wireless telecommunication is playing an increasing role in almost every field. With the spread of IoT and 5G technologies, all electronic devices will communicate over a network and millions of devices can be connected to each other over such network. Due to this, the number of base stations will also increase significantly. As a result, even more antennas will be installed both indoors and outdoors. It follows that the use of smaller and more compact antennas and simpler and more reliable parameter tuning are of great importance to service providers as well as to equipment manufacturers, both in terms of design and antenna selection. Metamaterials are sub-wavelength structures that act as a homogeneous material to create electromagnetic properties that would not be possible with conventional materials. With the help of today's modern design and manufacturing technologies, it is possible to implement and manufacture such structures. In this article, the theoretical background and application possibilities of periodic structures and materials are presented, followed by the tuning of a split ring resonator and its application on a patch antenna.

Keywords: Periodic structure, Metamaterial, Periodic filter, Antenna simulation

I. INTRODUCTION

Periodic structures are naturally occurring phenomena, one of the best examples being the minerals that are made of crystal structures [1]. As such, the crystal structures are made up of many small crystal elements that are identical to each other.

In microwave technology, periodic structures similar to crystal structures have also appeared [1]. These structures can be considered of finite, or even infinite elements, which can be in one-, two-, or three-dimensional shapes. The simplest example is the theoretical model presented in **Fig. 1**.

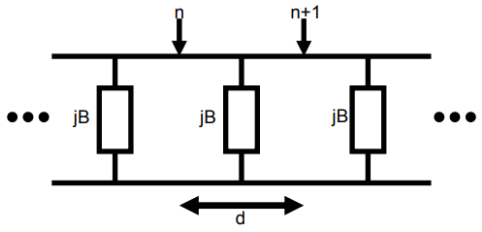

Figure 1. One-dimensional periodic structure [1]

II. ANALISYS OF THE PERIODIC STRUCTURE

The model of the periodic structure shown in **Fig. 1** consists of an infinite number of identical elements. Each element has a length *d*, in the center of which is the concentrated parameter *B* (joint to transmission line impedance) admittance.

If a concentrated parameter element is a two-port system, it can be described with a so-called ABCD matrix so that element is divided into three parts, a *d /2* length line, j*B*, and another *d/2* of the feed line. The relationship between input and output to *n-th* element is described by the equations (1-5)[2],

$$\begin{bmatrix} V_n \\ I_n \end{bmatrix} = \begin{bmatrix} A & B \\ C & D \end{bmatrix} \begin{bmatrix} V_{n+1} \\ I_{n+1} \end{bmatrix}, \quad (1)$$

$$A = \cos\theta - \left(\frac{b}{2}\right)\sin\theta, \quad (2)$$

$$B = j\left(\left(\frac{b}{2}\right)\cos\theta + \sin\theta - \frac{b}{2}\right) \quad (3)$$

$$C = j\left(\left(\frac{b}{2}\right)\cos\theta + \sin\theta + \frac{b}{2}\right) \quad (4)$$

$$D = \cos\theta - \left(\frac{b}{2}\right)\sin\theta \quad (5)$$

where θ = kd is the electric length of the feed line in the unit element, k is the wave number equal to the propagation coefficient of the TEM transmission line.

Assume, that the periodic structure is of infinite length, the wave parameters of the *n-th* and *(n + 1)* cells are identical, except for the phase shift caused by the propagation on the element. The equation in (1) can be reformulated as

$$\begin{bmatrix} V_n \\ I_n \end{bmatrix} = e^{-\gamma d}\begin{bmatrix} V_{n+1} \\ I_{n+1} \end{bmatrix}. \quad (6)$$

In eq (6) $\gamma = \alpha + j\beta$, which represents the complex propagation coefficient for the periodic structure. From (1) and (6) the following eigenvalue following simplification (eigenvalue) can be implemented:

$$\begin{bmatrix} A & B \\ C & D \end{bmatrix} = \begin{bmatrix} e^{-\gamma d} & 0 \\ 0 & e^{-\gamma d} \end{bmatrix}. \quad (7)$$

After further simplification

$$\cosh\gamma d = \cos\theta - \left(\frac{B}{2}\right)\sin\theta. \quad (8)$$

If $\alpha = 0$, then $\gamma = j\beta$, which leads to unattenuated wave propagation in the periodic structure. If the right side of the equation (8) is greater than one, no wave propagation occurs.

III. EXAMPLE FOR PERIODIC STRUCTURE

The capacitively loaded periodic structure behaves as follows from the point of view of wave propagation. (see an example in **Fig. 2**).

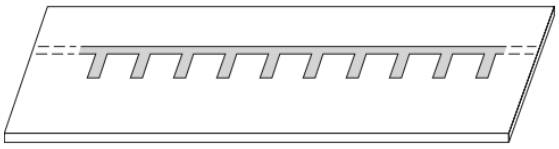

Figure 2. Microstrip periodic structure [2]

The concentrated parameter representation of the periodic structure in **Fig. 2** can be seen in **Fig. 3**

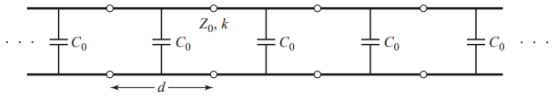

Figure 3. Theoretical model of a microstrip periodic structure [2]

The parameters of the structure are as follows: Z_0 = 50Ω, d = 1cm, C_0 = 2.6666pF. During this example, we define the k-β (Brillouin) diagram, the propagation coefficient, the phase velocity, and the Bloch impedance at f = 3GHz [2]. Replacing the dispersion ratio (6), gives the following relationship

$$\cos\beta d = \cos k_0 d - \left(\frac{C_0 Z_0 c}{2d}\right) k_0 d \sin k_0 d, \quad (9)$$

$$\cos\beta d = \cos k_0 d - 2k_0 d \sin k_0 d. \quad (10)$$

If the right side of the eq (10) is between 0 and 1, wave propagation will occur (passband-bandwidth). A Passband is created if it falls between $\theta \leq k_0 d \leq$ 0.96. The next passband is at π. Infinite number of passbands with decreased bandwidth may be achieved by increasing the $k_0 d$ value to infinity. At 3 GHz, $k_0 d$ takes the following value

$$k_0 d = 36^{\circ}. \quad (11)$$

It follows that βd is 1.5, so the propagation coefficient is β = 150 rad / m. The phase velocity is

$$v_p = \frac{k_0 c}{\beta} = 0.42c. \quad (12)$$

An important phenomenon is observed, showing that the phase velocity is much lower than the speed of light. These structures are called Slow-wave structures. From the above, the k-β (Brillouin) diagram can be determined.

Finally, the determination of Bloch impedance, which determines the wave impedance at the input of an element.

$$\frac{b}{2} = \frac{\omega C_0 Z_0}{2} = 1.256, \quad (13)$$

$$\theta = k_0 d = 36^{\circ}, \quad (14)$$

$$A = \cos\theta - \frac{b}{2}\sin\theta = 0.707, \quad (15)$$

$$B = j\left(\sin\theta + \frac{b}{2}\cos\theta - \frac{b}{2}\right) = j0.3479, \quad (16)$$

$$Z_B = \left(\frac{BZ_0}{\sqrt{A^2-1}}\right) = \left(\frac{(j0.3479)(50)}{j\sqrt{1-(0.0.707)^2}}\right). \quad (17)$$

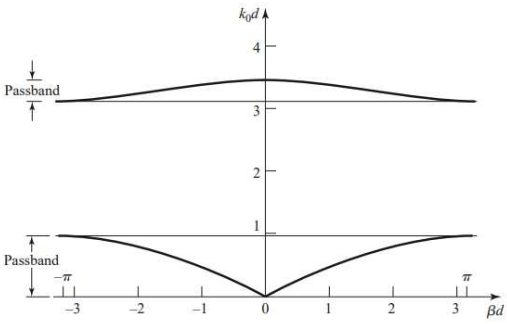

Figure 3. *k-β* (Brillouin) diagram [2]

IV. METAMATERIALS

Left-handed materials [3] are special artificial structures with negative refractive index (**Fig. 4**). The development of these materials is also emphasized in optical and microwave environments.

$$n_1 \sin(\theta_1) = n_2 \sin(\theta_2), \qquad (18)$$

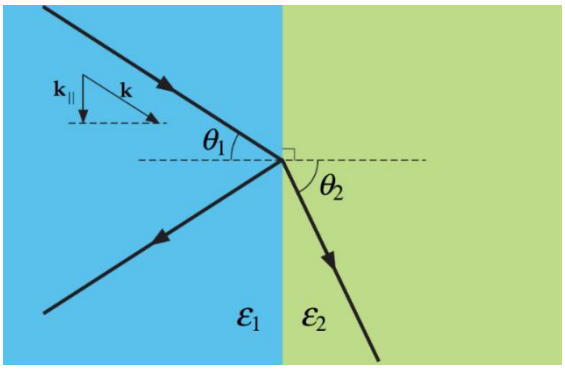

Figure 4. Refraction in a normal and a metamaterial [3]

In nature, substances generally have positive permittivity and permeability. However, there are also substances that have either negative permittivity or permeability. These properties are highly frequency dependent. $0>\varepsilon$ occurs in high frequency ranges, primarily in the optical range and in semiconductors from the THz range to the infrared range [2]. Examples of such materials are gold, silver, and aluminium.

In contrast, $\mu<0$ is available in a lower frequency range, typically in ferro- or antiferromagnetic materials. However, some metamaterials have recently been discovered, such as bismuth at $\lambda = 60$ μm. Unfortunately, bismuth cannot be used in practice due to its high resistance and relative rarity.

1. Electromagnetic metamaterials

Double Negative Metamaterials (DNG) [9] have both negative permeability and permittivity properties at the same frequency. This also means that they have a negative refraction index.

Metamaterial structures are often made of two kinds of Single Negative Metamaterials (SNG). SNG materials are closely related to Epsilon Negative Materials (ENG), with negative permittivity and positive permeability and to Mu-Negative Materials (MNG) with positive permittivity and negative permeability. The SNG structures have zero or close to zero positive properties, this is the difference between SNG and ENG/MNG. Two layers of different kinds of SNG can be combined to make an effective DNG material [8].

2. Split ring resonator

One solution is to create a material with the simultaneous use of two different periodic structures with different properties. An example of this is the combination of capacitive load strip and split-ring structures. The wire structure was electrically, while the split-ring structure was magnetically active at a given frequency. Metamaterials can be a big leap in the development of microwave technology. With their help, antennas can be designed more directional, more profitable, and smaller size antennas [6][13].

V. SIMULATION OF A SPLIT RING RESONATOR (SRR)

In this chapter, a simulation of a split ring resonator will be presented. The structure in **Fig. 5** was simulated at 12 GHz, its substrate is a 0.25mm thick FR4 epoxy.

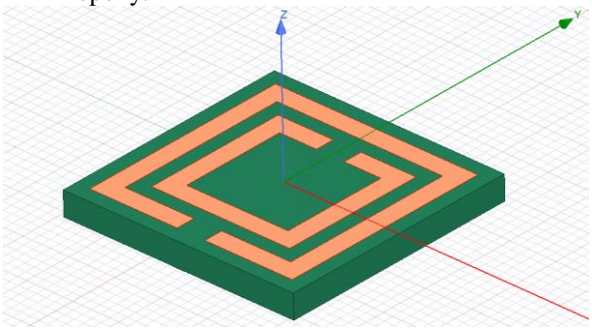

Figure 5. SRR element model in HFSS

The simulation has been performed using Ansys HFSS [5] simulation software in the frequency range of 5 - 15 GHz.

The simulation result in **Fig. 6** shows that the periodic structure operates as a DNG material. The structure has negative permeability and permittivity in the same frequency range. According to the results, the structure operates in the required 12 GHz frequency range and also has a quite wideband operation range with about 370 MHz.

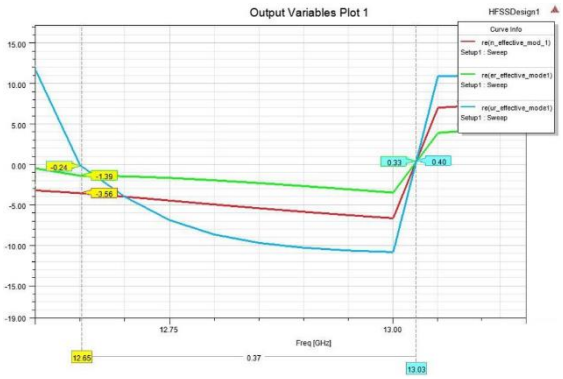

Figure 6. SRR element simulation results

VI. APPLICATION OF METAMATERIAL STRUCTURES

1. Metamaterial absorbers

Metamaterials can be used as radiofrequency absorbers. Their main advantage over conventional absorbers are suitable for miniaturization, effectiveness, wider frequency range and adaptability [4].

2. Metamaterial lenses

A refraction index that is close to zero is achievable with the use of periodic metamaterial structures. With zero refractive index, the structures behave like perfect lens. These lenses have optical, and microwave applications as well. As an optical device, it can replace glass as metamaterial lenses that are much thinner, lighter, and much more effective. In microwave technology, metamaterial lenses can be used to focus radiofrequency power, resulting in higher-gain antennas. Metamaterials can also be used for parabolic antennas, as their mode of operation is the same, but their size can be drastically reduced [9][10].

3. Metamaterial antennas

Metamaterials are used to increase the efficiency and minimize the size of antennas and antenna systems. Generally, metamaterials are used to increase the gain of conventional antennas using periodic structures. The antenna reflects part of the transmitted power back to the generator. With the use of periodic metamaterial structures, better impedance matching, improved gain, bandwidth, efficiency front-to-back ratio and so on can be achieved [5][11].

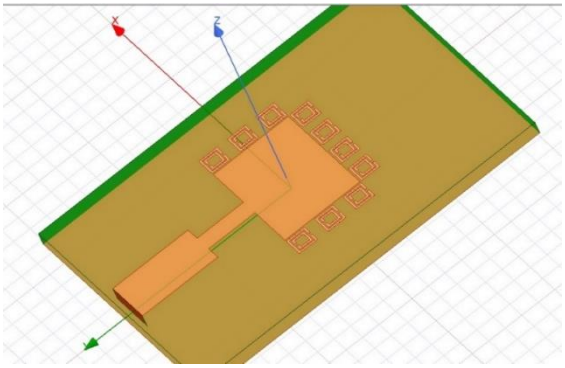

Figure 7. Experimental metamaterial patch antenna simulation in HFSS

The **Fig. 7** shows an early experiment to make a more efficient 10 GHz patch antenna. The patch of the antenna is surrounded by split ring resonators.

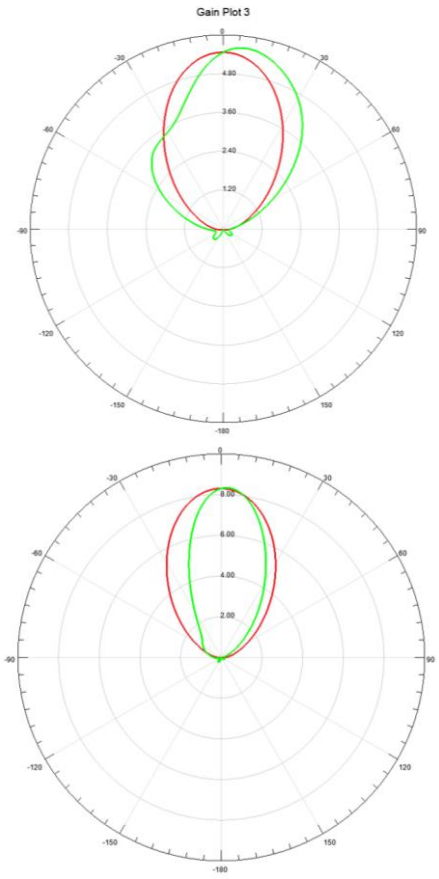

Figure 8. Experimental metamaterial patch antenna simulation Results

The simulation shows minor improvement in the antenna characteristics, better front-to-back ratio, and wider bandwidth. **Fig. 8** shows the difference in the antenna characteristic. The result on the left-hand side was made with the split ring resonators, meanwhile the characteristics shown on the right-hand side just the patch element was simulated. Using metamaterials, the gain of the patch antenna increased by 2.8 dB. The only drawback is that the reflection is 3 dB lower than in case of the regular patch antenna, but the difference can be neglected.

By tuning the split ring resonators, optimizing their placement around the patch element even better results may be achieved. This experiment showed that it is possible to improve the antenna parameters by adding metamaterial structures around the radiating patch. Additionally, the metamaterial structure created out of printed circuit adds no extra cost to the PCB. [7].

VII. CONCLUSION

The concept and the theoretical background of metamaterials have been presented. The practical applicability of metamaterials has been shown through an example with the goal of improving antenna characteristics. The results showed that some periodic structures can be used as

metamaterial, as it has a negative refractive index. SRR structures are very promising metamaterials, with further examination and optimization, they can be easily used in practice.

AUTHOR CONTRIBUTIONS

P. Prukner: Conceptualization, Theoretical analysis, Antenna simulation, Writing, Review and editing

M. Kuczmann: Supervision, Review and editing.

DISCLOSURE STATEMENT

We have no conflict of interest to declare.

ORCID

P. Prukner https://orcid.org/0000-0001-9444-4996

M. Kuczmann https://orcid.org/0000-0001-5042-7991

REFERENCES

[1] R. E. Collin, Foundations for Microwave Engineering, Second Edition, John Wiley & Sons, New York, 2001.

[2] D. M. Pozar, Microwave Engineering, Fourth Edition, John Wiley & Sons, New York, 2011.

[3] J. D. Joannopoulos, S. G. Johnson, Joshua N. Winn, R. D. Meade, Photonic Crystals: Molding The Flow Of Light, Princeton University Press, Princeton, 2008.

[4] G. Singh, Rajni, A. Marwaha, A Review of Metamaterials and its Applications, International Journal of Engineering Trends and Technology (IJETT) V19(6) (2015) pp. 305 – 310. https://doi.org/10.14445/22315381/IJETT-V19P254

[5] F. Capolino, Theory and Phenomena of Metamaterials, Taylor and Francis Group, LLC, Boca Raton, 2009.

[6] M. Gil, F. Aznar, A. Vélez, M. Durán-Sindreu, J. Selga, G. Sisó, J. Bonache F. Martín, Electrically small resonators for metamaterial and microwave circuit design, Passive Microwave Components and Antennas, Rijeka, 2010.

[7] C. Aroral, S. Pattnaik, R. Baral, SRR Inspired Microstrip Patch Antenna Array, Progress In Electromagnetics Research C 58 (2015) pp. 89 – 96. https://doi.org/10.2528/PIERC15052501

[8] N. Engheta, R. W. Ziolkowski, METAMATERIALS Physics and Engineering Exploration, John Wiley & Sons, New York, 2006.

[9] V. Verselago, L. Braginsky, V. Shklover, C. Hafner, Negative Refractive Index Materials, Journal of Computational and Theoretical Nanoscience V3 (2) (2006) pp. 189-218. https://doi.org/10.1166/jctn.2006.3000

[10] C. Y. Tan, K. T. Selvan, and V. Venkatesan, Performance Comparison of Pyramidal Horns Loaded with Metal Baffle or with Metamaterial, Progress In Electromagnetics Research C 17 (2010) pp. 131-144. https://doi.org/10.2528/PIERC09090907

[11] S. Zuffanelli, Antenna Design Solutions for RFID Tags Based on Metamaterial-Inspired Resonators and Other Resonant Structures, Springer international Publishing AG, Cham, 2018.

[12] Z. Hafdi, S. Zemouli, A. Chaabi, Retrieval of effective parameters of left handed materials by using different approaches, 2013 8th International Conference on Electrical and Electronics Engineering (ELECO) Bursa (2013) pp. 427-430. https://doi.org/10.1109/ELECO.2013.6713877

[13] P. G-Balmaz, O. J. F. Martin, Electromagnetic resonances in individual and coupled split-ring resonators, Journal of Applied Physics (2003) pp. 2929-2936. https://doi.org/10.1063/1.1497452

[14] D. R. Smith, S Schultz, P Markos, C M Soukoulis, Determination of effective permittivity and permeability of metamaterials from reflection and transmission coefficients, Physical Review B (2002). https://doi.org/10.1103/PhysRevB.65.195104

[15] Z. Hafdi, S. Zemouli, A. Chaabi, Retrieval of effective parameters of left handed materials by using different approaches, 2013 8th International Conference on Electrical and Electronics Engineering (ELECO) Bursa (2013) pp. 427-430. https://doi.org/10.1109/ELECO.2013.6713877

[16] P. G-Balmaz, O. J. F. Martin Electromagnetic resonances in individual and coupled split-ring resonators, Journal of Applied Physics (2003). https://doi.org/10.1063/1.1497452

ACTA TECHNICA JAURINENSIS
Vol. 15, No. 4, pp. 193-198, 2022
10.14513/actatechjaur.00680

Improvement of mechanical properties of recycled PET by reactive toughening and post-crystallization

Emese Slezák[1], Ferenc Ronkay[2], Katalin Bocz[1,*]

[1]Department of Organic Chemistry and Technology,
Budapest University of Technology and Economics, Műegyetem rkp. 3., H-1111 Budapest, Hungary
[2]GAMF Faculty of Engineering and Computer Science,
John von Neumann University, Izsáki út 10, H-6000, Kecskemét, Hungary
*e-mail: bocz.katalin@vbk.bme.hu

Submitted: 28/09/2022 Accepted: 24/10/2022 Published online: 26/10/2022

Abstract: Noticeable increase in impact strength of recycled PET (RPET) was achieved using ethylene-butyl acrylate-glycidyl methacrylate (EBA-GMA) type reactive terpolymer (PTW). The decrease in stiffness and heat resistance due to reactive toughening was successfully compensated by thermal annealing. Based on the results, strong correlation can be shown between crystallinity and impact strength: increasing crystallinity results in reduced impact resistance at PTW contents higher than 5 m/m%, yet a 6-time increase compared to 100 % crystallized RPET was reached with 15 m/m% PTW content. Regarding heat resistance and stiffness, crystallinity appears to be the key parameter: above a critical value of 10 % crystallinity a sharp improvement of the properties can be noticed. Based on the results, properly choosing the elastomer ratio and post-crystallization conditions, post-consumer PET can be suitable for durable engineering applications as well.

Keywords: recycling; poly (ethylene terephthalate); reactive toughening; crystallization

I. INTRODUCTION

Poly (ethylene terephthalate) (PET) is one of the commodity plastics that are applied in the largest quantity: in 2020, 70 million tonnes was produced [1]. One of its main applications is the packaging industry where plastic bottles are produced, which after a short life cycle become waste. Annually 1.4 – 1.6 billion PET bottle waste is generated, from which only 35% is recycled [2]. Its application as a durable engineering plastic, however, is limited, due to its brittleness and the low heat resistance in amorphous phase.

Semi-crystalline PET has a low impact resistance therefore it fades to the background in the engineering plastic fields. Toughening is a possible solution for this problem, which can be carried out by compounding the polymer with elastomers, or by copolymerization [3]. Billon and Meyer [4] studied the toughening of amorphous and semi-crystalline PET with core-shell particles. For their experiments, high-intrinsic-viscosity (IV) PET and two core-shell particles were used. The latter have similar chemical structures: butyl acrylate core and PMMA shell. One of the toughening agents had reactive epoxy groups on their shell to promote the linkage of elastomer and PET ends of chain, while the other agent did not contain reactive groups. Based on their research, it can be concluded that the toughening effect of core-shell nodules is based on the formation of cavitation voids, which cause local disturbance in the stress field of the sample, so plastic deformation or other energy dissipating fracture mechanism occurs. It is important to note, that while both elastomer systems could successfully toughen amorphous PET, the effective toughening of semi-crystalline polymer was only possible with sufficient adhesion and homogenous dispersion of the elastomer particles, which can only be achieved by reactive toughening.

In another study Bocz et al. [5] examined the effect of the molecular weight (MW) of PET matrix on the toughening efficiency. By applying recycled PET (RPET), the increased number of reactive terminal groups and shorter, but more mobile chains enable to reach prominent impact strength with lower elastomer content (10 m/m%), while original PET requires higher ethylene-butyl acrylate-glycidyl methacrylate (EBA-GMA) content. Short-chained, reactive RPET molecules provide better dispersion of the elastomer, as more chemical bounds can be formed between the polymer and the toughening agent. Even though impact strength greatly

improves, other mechanical properties (stiffness) decreases. Continuing the previous study, Ronkay et al. [6] analysed the impact of the water content of PET on toughening, and noticed that a certain amount of water during melt processing promotes hydrolytic degradation which creates the reactive, short-chained PET fraction that is necessary for effective reaction with EBA-GMA. As a result, almost 6 times higher notched impact strength was achieved simply by omitting the conventional drying step before processing the polyester.

PET can be crystallized due to its chemical and geometrical regularity. The crystallinity and the morphology of the structure strongly effects the polymer's properties. Higher crystallinity results in higher glass transition temperature (T_g): the T_g of amorphous PET is 65-70 °C, while the semi-crystalline PET's T_g is 15-20 °C higher than that. Besides, semi-crystalline polymers have higher modulus, tensile strength, hardness and have higher resistance against solutions, but their impact properties are poor [7].

Loyens and Groeninckx [8] examined the effect of matrix properties (MW, crystallinity) and temperature on the impact resistance of elastomer toughened semi-crystalline PET. The dispersed phase was ethylene-propylene copolymer (EPR), besides, ethylene and 8 m/m% glycidyl-methacrylate (E-GMA8), latter served as a compatibilizing agent. When no compatibilizer was applied, the structure was rough, regardless the MW. E-GMA8 significantly reduced the size of the dispersed phase, but further increasing its ratio did not lead to notable change at low and medium MWs. In contrast, high MW materials showed stronger dependence on dispersed phase concentration and composition. Latter can be explained by the reduced number of end-groups, which results in fewer interfacial grafts.

It can be concluded, that the MW of the matrix significantly affects both crystallization and PET-GMA interaction [5,8]. RPET is more favourable from both aspects than original PET, because of the short-chained fraction. The proper dispersion of the elastomer particles and the developing morphology are key to sufficient toughening: the finer the structure, the better the impact resistance. Crystallinity affects both mechanical and thermal properties, moreover the ratio of rigid amorphous phase also influences the properties according to the three-phase model [9].

Previous studies proved that RPET can be toughened by EBA-GMA type terpolymer (PTW) PTW more effectively and better impact strength results can be achieved compared to original PET [5], however stiffness and rigidity decreases. The aim of the study is to simultaneously improve impact resistance and stiffness with PTW and post-crystallization. By optimizing the mechanical properties of RPET, new, potential application areas will open, thus it can be a promising alternative to structural polymers such as acrylonitrile butadiene styrene (ABS) or polycarbonate (PC).

II. MATERIALS AND METHODS

As for the recycled material, industrial quality recycled PET flakes (RPET) were applied (JP Pack Kft., Hungary), which had 0.56 ± 0.03 dl/g IV value and M_w = 16 900 g/mol, as measured by GPC [5]. The recycled polymer was from packaging used in food industry: the grinded excess material from sheet extrusion and thermoforming. As toughening agent, Elvaloy PTW (DuPont, USA) (PTW) which consists of 66.75 m/m% ethylene, 28.00 m/m% butyl acrylate and 5.25 m/m% glycidyl methacrylate, was applied as reactive toughener. The melt flow index of PTW is 12 g/10 min (190 °C / 2.16 kg), its melting point is 72 °C and has a glass transition temperature at -55 °C [10]. Based on our previous research [5], PTW was applied in RPET matrix at 0, 5, 10 and 15 m/m%, respectively.

Compounding was carried out by LTE 26 - 48 (Labtech Scientific, Thailand) type, twin-screw extruder. The polymer was dried for 3 hours at 160°C prior to processing, then the temperature was lowered to 90 °C and the PET was dried for additional 1 hour. Decreasing the drying temperature was necessary to prevent the premature melting of PTW. Zone temperatures varied from 250°C to 260°C, and the screw speed was 90 rpm with 40% relative engine performance. The processing parameters (zone and die temperatures, screw speed) during compounding were kept constant at each composition. It can be observed in Table 1, that under these conditions the die pressure increased linearly with increasing PTW content, which indicates chemical reaction taking place between the blend components. However, changing the processing conditions was not necessitated.

Table 1. *Die pressures during compounding*

PTW content (%)	***Die pressures (bar)***
0	43
5	47
10	49
15	56

After 4 hours of drying the granules were injection moulded 60 mm x 60 mm x 2 mm plaques by Mitsubishi 50MetII injection moulding machine. The zone temperatures changed from 245 °C to 255 °C and the mould temperature was 40 °C. holding pressure was 50 MPa and lasted for 4 s.

The injection moulded plaque specimens were annealed at a preheated Memmert Une 200 drier, at 150°C, between two aluminium mould plates for 180 s.

10 mm wide specimens were cut from the injection moulded plaques, notched, and tested by Izod impact tester at room temperature. Pendulum energy was 5.5 J, and the no-load loss was 0.02 J.

The quasi amorphous and semi-crystalline samples were examined by DSC in nitrogen atmosphere. The temperature ranged from 20°C to 320°C and the cooling rate was 20°C/min. The original crystallinity of the material was determined from the heating curve in accordance with the following equation (1):

$$CRF = \frac{\Delta h_m - \Delta h_{cc}}{\Delta h_m^0 \cdot (1 - w_{PTW})} \cdot 100\% \qquad (1)$$

Where CRF (%) is the calculated crystallinity, Δh_m (J/g) is the area of the mass specific melting peak, Δh_{cc} (J/g) is the area of the mass specific cold crystallization peak, Δh_{m0} (J/g) is the mass specific enthalpy of 100% crystalline PET and w_{PTW} (-) is the weight ratio of PTW.

Dynamic mechanical analysis (DMA) in tensile mode was performed on the 30 mm x 8 mm x 2 mm specimens with 10 Hz frequency. The temperature ranged from 10°C to 140 °C, and the heating rate was 3 °C/min. The distance between the grips was 20 mm.

III. Results and Discussion

1. Effects of the elastomer content and thermal annealing on the mechanical properties

PTW is a well-known toughening agent, which has already been applied to PET blends successfully [5,6]. The notched Izod impact strength of the RPET samples with increasing PTW contents before and after crystallization are presented in **Fig. 1**.

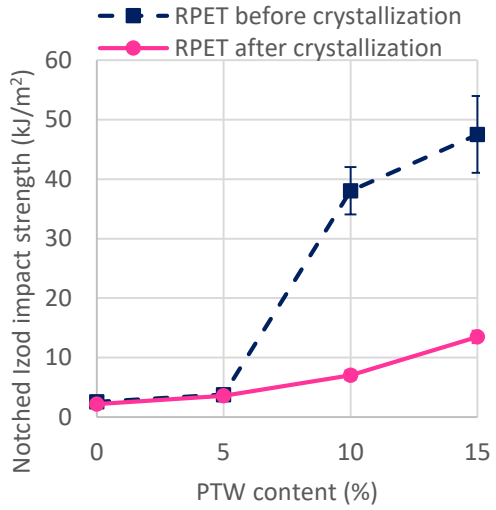

Figure 1. *Notched Izod impact strength as the function of PTW content*

The elastomer is efficient for the amorphous samples above 10 m/m% of PTW, where a sharp increase in the impact strength can be seen. The results further improve with the addition of 15 m/m% PTW. This can be explained by the short chains in RPET which form an effective toughening enhancer interphase [5] in the presence of the reactive elastomer. The crystallized specimens show a different tendency: the impact strength gradually increases with increasing elastomer ratio. Crystallization clearly effects the impact resistance above 5 m/m% PTW content, as the values decrease by 75 % after crystallization, but with 15 m/m% PTW content the impact strength is still 6-times higher than that of 100 % crystallized RPET. At lower elastomer ratios impact strength barely changes.

Fig. 2 illustrates the storage modulus at room temperature (23°C) as the function of PTW content. A decreasing linear correlation between the two parameters can be observed. After crystallization the parameters still show linear correlation. Compared to the amorphous samples, a 20 % increase in storage moduli can be seen, which means that the post-crystallization improved the stiffness.

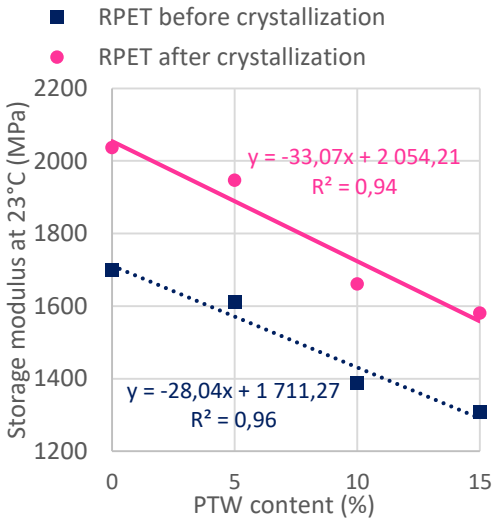

Figure 2. *Storage modulus (23°C) as the function of PTW content*

Storage modulus at 90°C is in connection with the heat resistance of the material. These values are presented as the function of PTW content in **Fig. 3**. Before crystallization the storage moduli are relatively low (between 4-8 MPa), but a great enhancement can be achieved by the 3-minute crystallization. As a result, the storage moduli values reach 400 – 600 MPa, which is a two orders of magnitude increase. The elastomer content significantly decreases the stiffness, as **Fig. 2** and **Fig. 3** show it.

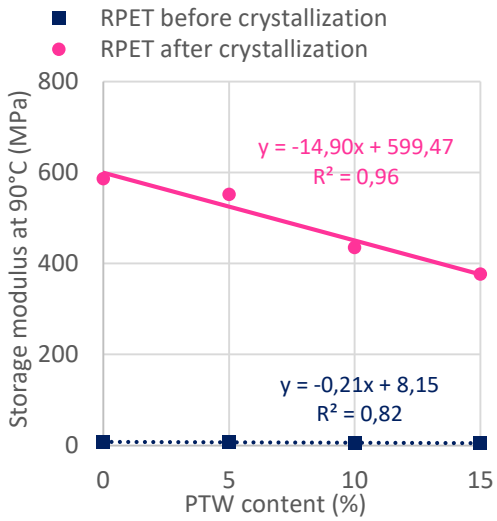

Figure 3. *Storage modulus (90°C) as the function of PTW content*

2. Effect of the elastomer content and the post-crystallization on the morphology

Crystallinity was determined by DSC analysis, and the results are presented in **Fig. 4**. Before the crystallization the value of initial crystallinity is between 8 - 10 %, which is not significantly influenced by the PTW content. However, after the crystallization the values moderately increase with the PTW content from 24 to 26%. This indicates that PTW does not really affect the crystallization process. The crystallization time appears to be efficient: the crystallized 100 % RPET has appr. 17 % increase in relative crystalline fraction.

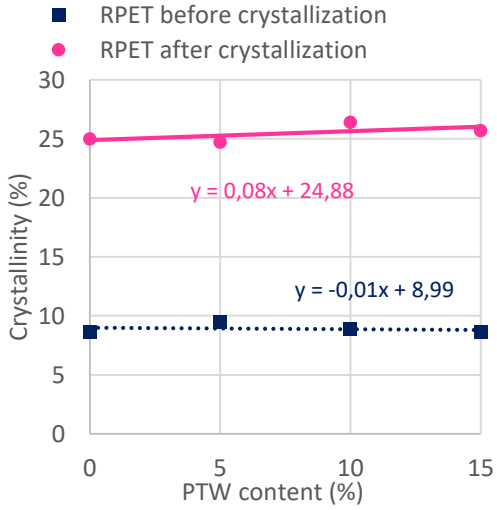

Figure 4. *Crystallinity as the function of PTW content*

Fig 5 presents the glass transition temperatures (T_g) as the function of PTW content. A slight decrease in the values can be observed as more elastomer is added to the samples. However, thermal annealing has a more significant effect, as T_g increases by 15°C after crystallization.

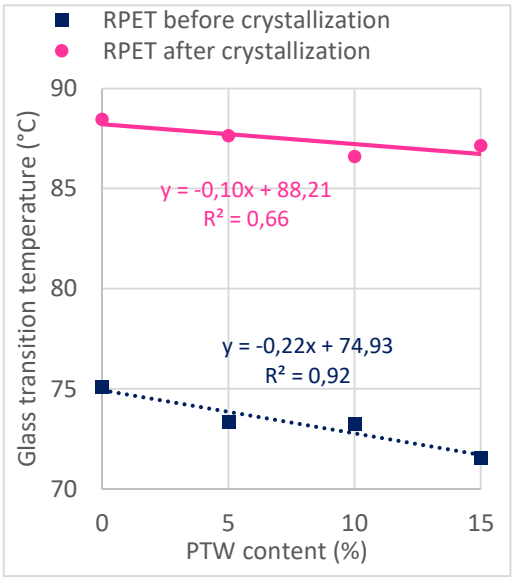

Figure 5. *Glass transition temperature as the function of PTW content*

Fig. 6 shows the connection between storage modulus (at 23°C) and crystallinity. Samples with the same PTW content have a great difference in their storage modulus. The performance of the ones with higher crystallinity is much better: the improvement is appr. 300 MPa.

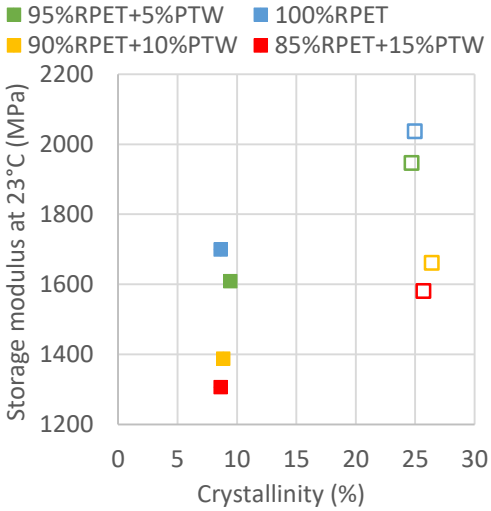

Figure 6. *Storage modulus (23°C) as the function of crystallinity: before crystallization: ■, after crystallization: □*

Fig 7 shows a similar trend: the storage moduli at 90°C are lower when the crystallinity is below 10 %, and a sudden, significant increase can be noticed at higher crystallinity rates. **Figs. 6** and **7** suggest that a critical crystallinity level is required to achieve enhanced stiffness and heat resistance.

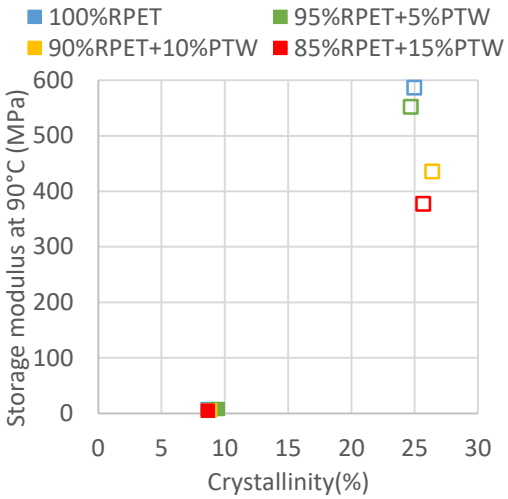

Figure 7. *Storage modulus (90°C) as the function of crystallinity: before crystallization: ■, after crystallization: □*

Notched Izod impact strength significantly decreases with crystallinity if the PTW content is 10 m/m% or higher, as it is indicated in **Fig. 8**. At lower elastomer ratios the initial impact resistance does not change significantly with crystallinity.

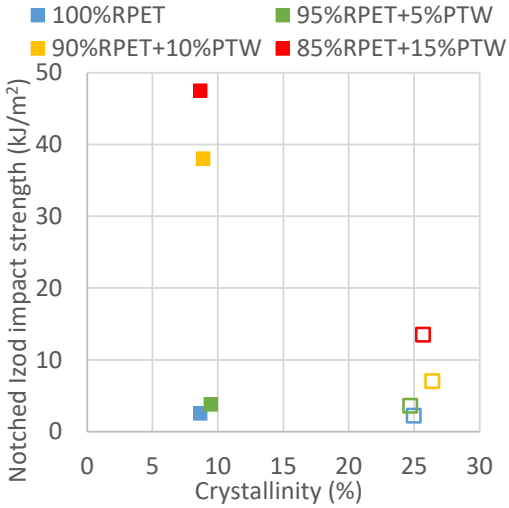

Figure 8 *Notched Izod impact strength as the function of crystallinity: before crystallization: ■, after crystallization: □*

Fig. 9 shows that the impact strength is inversely proportional to the storage modulus at 23°C. Crystallized samples have relatively high storage moduli, while the uncrystallized ones with higher PTW content, have outstanding impact resistance.

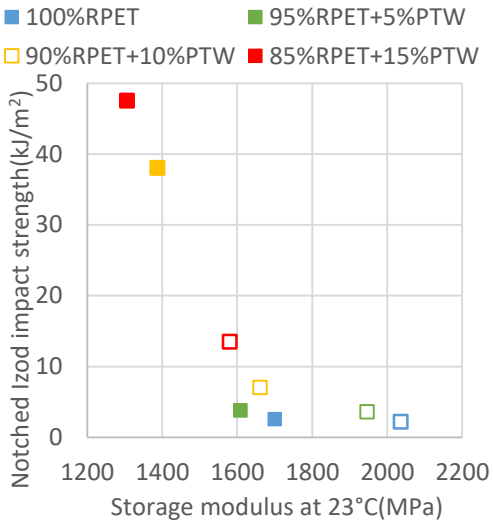

Figure 9. *Notched Izod impact strength as the function of storage modulus (23°C: before crystallization: ■, after crystallization: □)*

IV. Conclusions

For successful toughening of RPET, at least 10 m/m% PTW is required, which results in a 15-fold increase in impact strength compared to 100 % RPET. 15 m/m % PTW provides an even better toughening, with almost 19 times better results. After thermal annealing, storage moduli at 23°C increased by 250-300 MPa, and by 70 times at 90°C. By post-crystallizing the samples at 150°C for 3 minutes each composition reached 24 – 26 % crystallinity. Annealing deteriorates the effect of PTW, and impact resistance values decrease compared to the non-crystallized samples. However, higher PTW contents still resulted in better toughening properties. Even though post-crystallization decreased impact resistance, it greatly enhanced stiffness and heat resistance.

Based on the results, altering the additive ratio and the post-crystallization, it is possible to develop heat-resistant and stiff injection moulded PET products from bottle scrap, with balanced toughness, thus suitable for engineering applications.

V. Acknowledgement

The publishing of this paper was supported by the National Research, Development and Innovation Fund of Hungary in the frame of the 2019–1.3.1-KK-2019–00004 and GINOP_PLUSZ-2.1.1-21-2022-00041 projects. The research was funded by the Hungarian Scientific Research Fund, grant number FK128352.

AUTHOR CONTRIBUTIONS

E. Slezák: Experiments

F. Ronkay: Conceptualization, analysis of the results

K. Bocz: Supervision, Review and editing.

DISCLOSURE STATEMENT

The authors declare that they have no known competing financial interests or personal relationships that could have appeared to influence the work reported in this paper.

ORCID

Ferenc Ronkay: https://orcid.org/0000-0003-0525-1493

Katalin Bocz: https://orcid.org/0000-0003-3912-1013

REFERENCES

[1] L. Dai, Y, Qu et al., Enhancing PET hydrolytic enzyme activity by fusion of the cellulose-binding domain of cellobiohydrolase I from *Trichoderma reesei*, Journal of Biotechnology 334 (2021) pp. 47-50. https://doi.org/10.1016/j.jbiotec.2021.05.006

[2] C. Kutasi, A PET palack és egyéb poiészter hulladékok újrafeldolgozása, újrahasznosítása, Kaleidoscope History 11 (2021) pp. 50–58, in Hungarian. 10.17107/KH.2021.22.294-304

[3] V.A. Szabó, G. Dogossy, Structure and properties of closed-cell foam prepared from rPET, IOP Conference Series: Materials Science and Engineering 426 (1) (2018) 012043. https://doi.org/10.1088/1757-899X/426/1/012043

[4] N. Billon, J. P. Meyer, Experimental study of rubber-toughening of pet, European Structural Integrity Society 32 (2003) pp. 65-75.

[5] K. Bocz, F. Ronkay et al., Application of low-grade recyclate to enhance reactive toughening of poly (ethylene terephthalate), Polymer Degradation and Stability 185 (2021) https://doi.org/10.1016/j.polymdegradstab.2021.109505

[6] F. Ronkay, B. Molnár et al., Water boosts reactive toughening of PET, Polymer Degradation and Stability 203 (2022) https://doi.org/10.1016/j.polymdegradstab.2022.110052

[7] B. Demirel, A. Yaraş, and H. Elçiçek, Crystallization behaviour of PET materials, BAÜ Fen Bil. Enst. Derg 13 (2011).

[8] W. Loyens, G. Groeninkx, Rubber toughened Semicrystalline PET: Influence of the matrix properties and test temperature, Polymer 44 (2002) pp. 123-136. https://doi.org/10.1016/S0032-3861(02)00743-7

[9] J. D. Badia, E. Strömberg, The role of crystalline, mobile amorphous and rigid amorphous fractions in the performance of recycled poly (ethylene terephthalate) (PET), Polymer Degradation and Stability 97 (2012) http://dx.doi.org/10.1016/j.polymdegradstab.2011.10.008

[10] Y. Yuryev, A. K. Mohanty and M. Misra, Hydrolytic stability of polycarbonate/ poly (lactic acid) blends and its evaluation via poly(lactic) acid median melting point depression, Polymer Degradation and Stability 134 (2016) pp. 227-236. http://dx.doi.org/10.1016/j.polymdegradstab.2016.10.011

ACTA TECHNICA JAURINENSIS
Vol. 15, No. 4, pp. 199-206, 2022
10.14513/actatechjaur.00681

Parametric analysis of the stress-strain state for the unsupported and supported horizontal underground workings

Oleksii Tiutkin[1,*], Nataliia Bondarenko[1]

[1]Department «Transport infrastructure», Ukrainian State University of Science and Technologies
Lazaryan Str., 2, Dnipro, 49010, Ukraine
*e-mail: o.l.tiutkin@ust.edu.ua

Submitted: 01/10/2022 *Accepted: 25/10/2022* *Published online: 26/10/2022*

Abstract: An analysis of analytical and numerical approaches to the problem of determining the stress-strain state of underground workings has been carried out. A system of parametric analysis of the stress-strain state of unsupported and supported horizontal underground workings has been developed. This system proved that to determine the stress-strain state of horizontal unsupported workings of a certain diameter, it is enough to perform one numerical calculation of a finite-element model with unit parameters, and using simple analytical formulas, extrapolate the stress-strain state of this model to all possible cases of real workings. Finite element models of underground workings were developed to justify the author's system. A method of parametric analysis of the strained state of a supported working by using models with equivalent bending stiffness has been developed and substantiated. On its basis, it is possible to perform a numerical analysis of a finite-element model with unit parameters of the frame, selecting the equivalent modulus of elasticity.

Keywords: finite element modelling; horizontal underground working; parametric analysis; rock massif; stress-strain state

I. INTRODUCTION

In geomechanics, two conceptual directions in the research of the stress-strain state of horizontal underground workings have been formed and are further developing: 1. It is based on an analytical approach; 2. It is based on numerical methods. Reviews in the application of these directions conducted by many researchers [1-3] allow us to highlight their inherent features, wherein these features are most often the advantages and disadvantages of calculation methods.

For example, methods based on an analytical approach are noted by the universality of solutions that can be applied to different conditions, but their disadvantage is a significant number of assumptions introduced when obtaining [3, 4]. Numerical methods, in turn, are characterized by the possibility of calculating many complex underground facilities [5-7]. But their disadvantage is that the obtained solutions refer to specific calculation cases and cannot be extrapolated to similar cases with changed properties [1, 3, 6].

Recently, analytical methods have been much less often used in the calculations of underground facilities, which are explained by the complexity of their application (complicated mathematical apparatus, insufficient software implementation, etc.). A weighty argument for applying numerical methods is a specific approach to each underground facility. This approach is more expedient and rational than a typical calculation without taking into account the specific characteristics of the behavior of an underground structure.

The finite element method is the most widely used numerical method today [3, 5-9]. Its large-scale application is explained by the development of theoretical foundations, the simplicity of algorithmization, and the availability of powerful professional calculation complexes. However, at the same time, in applying the finite element method in the calculations of underground facilities, including horizontal workings, there was a gradual separation from the methodology developed by analytical methods, which led to some one-sided research in this direction [8-11]. It is due to the finite element method's specific features since obtaining high-accuracy solutions; the adequate finite-element model should be developed for real conditions. The mentioned feature of the finite element method (the impossibility of extrapolating the numerical solution

of a specific problem to another one with somewhat changed characteristics) is proclaimed by some authors who tend towards an analytical approach as a methodological drawback. However, obtaining a sufficiently accurate solution for a specific calculation case is sometimes more important than obtaining a dependence that can be applied to other cases.

Undoubtedly, the knowledge of the mechanisms for forming the stress-strain state in the "horizontal working – rock massif" system is a key issue of geomechanics. The currently existing methods in studying the stress-strain state are a set of disembodied methods for calculating individual components of stresses and strains, which can be applied only in limited research conditions. Such a situation, in many cases, does not allow obtaining a quantitative picture of the distribution of the stress-strain state in the "horizontal working – rock massif" system. Therefore, a new methodological technique is needed to solve this problem, which allows performing operational determination of the stress-strain state for horizontal working.

II. METHODS

Such a methodological technique is parametric analysis developed by the authors based on numerical analysis using the finite element method [3, 8, 9]. Within the framework of this article, the parametric analysis as the research of the stress-strain state of a horizontal working is understood, during which a specific numerical solution is extrapolated to other calculation cases using the author's algorithms. Exactly these algorithms help solve the issue of the imaginary impossibility of distributing a numerical solution, which is declared by authors who tend toward clear analytical solutions. However, the parametric analysis does not break links with the analytical approach [10, 11].

It is known that representatives of the analytical approach often ground their solutions for horizontal underground workings on the theoretical patterns of Kolosov-Mushkelishvili's theory of functions of a complex variable, that is, one of the theories of continuum mechanics [3, 7]. In practice, this theory is implemented using conformal mappings, the essence of which is as follows. The real working of any delineation with a defined specific radius R by means of direct mapping turns into a circular working with a unit radius, to which the patterns of Kolosov-Mushkelishvili's theory are applied. Then, after obtaining the solution of the stress-strain state on a circular working with a unit radius, it is extrapolated to a real working with a defined specific radius R by means of inverse conformal mapping.

A critical analysis of this approach proves that a powerful mathematical apparatus is needed to obtain them, which is most often not implemented in software complexes. However, the very conceptual procedure of Kolosov-Mushkelishvili's theory is fruitful. Its reinterpreting in line with numerical solutions is that the stress-strain state on a circular working with a unit radius and with the help of special parameters can be extrapolated to other workings. Thus, it is possible to obtain a solution for the stress-strain state on the working with a unit radius without applying complex direct and inverse conformal mappings by scaling the properties of the system [10, 11].

Unquestionably, the application of scaling for unsupported and supported workings with some similarities in the methodology still differs in both theoretical and practical terms. This is an objective position, since the presence of a frame, which is constructed in an unsupported working, radically changes the stress-strain state in the "horizontal working – rock massif" system. The engineering structure/the rock massif interaction is considered to be the basic principle of geomechanics, but its appearance makes the task of searching for the stress-strain state as difficult as possible.

For the research objectives, a basic finite-element model of the "horizontal working – rock massif" system is developed, which consists of rectangular and square finite elements and maximally reflects the geometry of the working (**Fig. 1**).

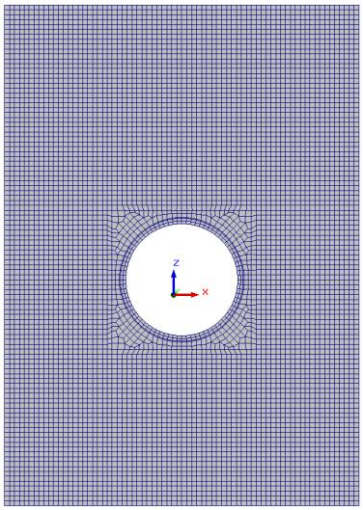

Figure 1. *The finite-element model for the "horizontal working – rock massif" system*

The authors will use the developed models with unit parameters for the primary parametric analysis, implemented with the professional complex SCAD. In these models, the geometric parameters of the underground working are accurately reflected, and the modulus of elasticity E and the density of the rock or soil γ are equal to one. It should also be noted that all further solutions are implemented in an elastic approach since the elastic-plastic solution is quite difficult to solve [12].

The finite element model is a spatial one based on volumetric finite elements. The number of nodes of the model is 5268 pieces, finite elements are 3288 pieces. Model dimensions: height is 20 m, width is 22 m, thickness is 1 m. All nodes of the model are common, and the dimension of finite elements is from 0.25×0.25 to 0.5×0.5 m, which for a model with such dimensions is sufficient to obtain sufficiently accurate results.

Since the stress-strain state of the system changes dramatically while installing fasteners into a horizontal working, it is impossible to conduct a primary parametric analysis of the stress-strain state in a similar way as for an unsupported working. For supported working, a secondary parametric analysis should be conducted proceeding from other initial parameters. This is explained by the fact that the frame is made of different materials (concrete, reinforced concrete, cast iron) and has a thickness range (for horizontal workings with a diameter of 5.6 … 6 m, a thickness of h=0.15 … 0.3 m). Therefore, any change in the parameters of the frame reshapes the stress-strain state in the "horizontal working – rock massif" system, and there are still no final analytical solutions for the distribution of stress and strain components for all possible cases.

In this research, the authors introduce the following proposal, which allows for evaluating the deformed state of a horizontal supported working when there is a change in the thickness of the frame and its material. The controlling parameter affecting the change in displacements of the "horizontal supported working – rock massif" system is both the thickness h and width b of the fastening and to a greater extent the bending stiffness EI. This parameter is integral because it binds the deformation property of the frame material (modulus of elasticity E) and its geometric dimensions (moment of inertia $I = bh^3/12$).

As can be seen from the parametric analysis of the "horizontal supported working – rock massif" system, a stressed state is derived, which is explained by objective reasons. Even if the real deformation characteristics of the rock massif (modulus of elasticity E_r and Poisson's ratio μ_r) is accepted as constant for all possible calculation cases, then the change in the geometric parameters of the fastening (thickness h and width b) leads to a significant change in the stress components. This is due precisely to the change in the interaction between the fastening and the rock massif, which adjust to each other, creating an almost unique stress state for calculated cases with slightly varied thickness h.

Thus, if the bending stiffness EI is taken as the controlling deformation parameter, the following calculation situation can be considered. For two frames of a running tunnel with an inner diameter of 5.1 m and made of different materials (reinforced concrete and cast iron), the equality $E_1 I_1 = E_2 I_2$ must be:

$$E_1 \frac{b_1 h_1^3}{12} = E_2 \frac{b_2 h_2^3}{12}, \quad (1)$$

which is simplified if the width b is chosen to be the same for two frames (b =1.0 m).

Accordingly, the task, with the help of a somewhat artificial technique, introduced only to simplify it, returns to the search for an equivalent thickness of the frames. However, it should be emphasized that in the general case where the frame width b may not be the same (1.0 m for cast iron frame and 1.2 m for reinforced concrete blocks), the bending stiffness EI remains the controlling parameter. Having set the modulus of elasticity (for cast iron is E_1=20.1·10^4 MPa and reinforced concrete is E_2=32.5·10^3 MPa) and solved equation (1), Eq.(2) is obtained:

$$h_2 = \sqrt[3]{\frac{12 E_1 I_1}{E_2}}. \quad (2)$$

Accordingly, if the thickness of the cast iron frame h_1=0.15 m is set, the equivalent thickness of the reinforced concrete frame will be equal to h_2=0.275 m (**Fig. 2**).

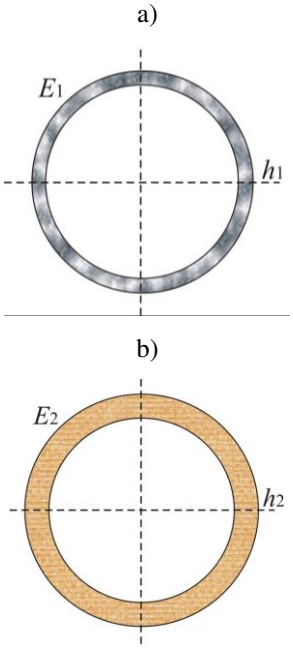

Figure 2. *Schemes of supported horizontal working with an internal diameter of 5.1 m and equivalent EI: a) thickness is of h_1=0.15 m (cast iron); b) thickness is of h_2=0.275 m (reinforced concrete)*

For these two calculation cases, the basic finite-element model (**Fig. 1**) has been modified, since the working is supported. Finite element models are created spatial ones based on volumetric elements. The number of nodes in the model is 18912 (cast iron) and 23156 (reinforced concrete); of finite elements is 9216 (cast iron) and 11316 (reinforced concrete). All nodes in the model are common, the dimension of the finite elements is from 0.12×0.12 m to 0.15×0.18 m. These dimensions are sufficient to obtain an accurate solution to the set task.

III. RESULTS AND ITS ANALYSIS

After creating finite-element models for unsupported and supported workings, a numerical analysis of each of them has been carried out. Below are the results on the research of the finite-element model for the unsupported working with unit parameters (**Fig. 3-4**).

a)

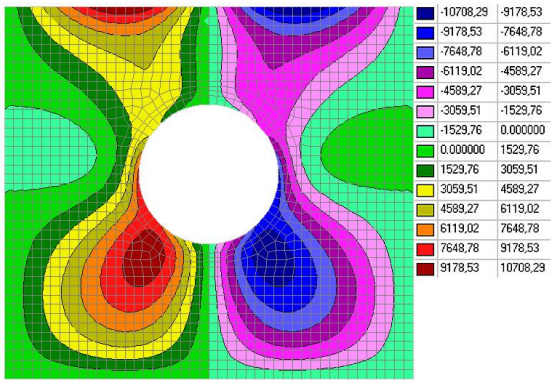

b)

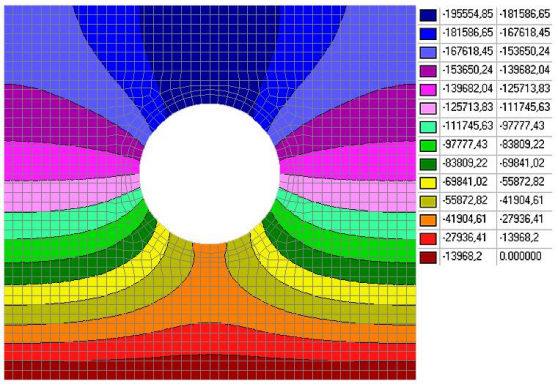

Figure 3. *The strained state of the finite-element model with unit parameters: a) displacement along the horizontal axis; b) displacement along the vertical axis*

Having obtained the distribution of isopoles of stresses and displacements in the model with unit parameters, it is quite easy to move to the real case using the author's algorithm of primary parametric analysis:

a)

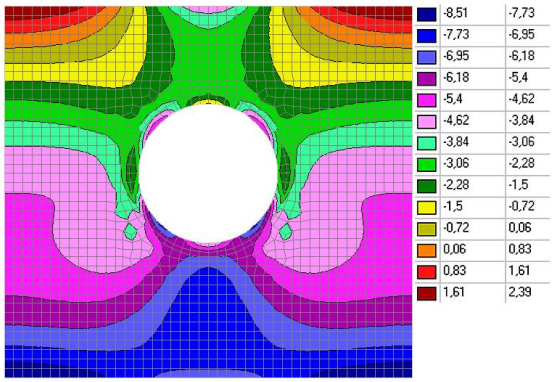

b)

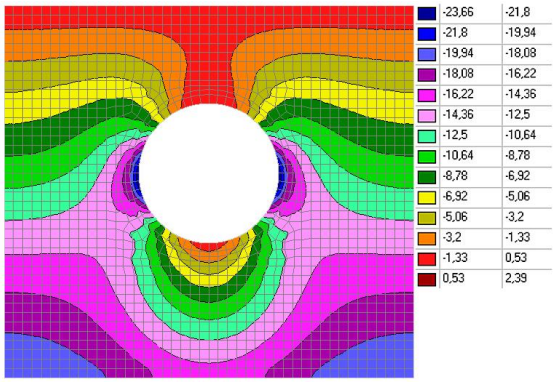

Figure 4. *The stress state of the finite-element model with unit parameters: a) stress along the horizontal axis: b) stress along the vertical axis*

1) to obtain real displacements S_r, the displacement in the model with unit parameters S_e should be multiplied by the value of the real specific gravity γ_r and divided by the real value of the modulus of elasticity E_r and the unit value of the specific gravity:

$$S_r = S_e \frac{\gamma_r}{E_r}; \quad (3)$$

2) to obtain the real stress σ_r , the stress in the model with unit parameters σ_e should be multiplied by the value of the real specific gravity and divided by the unit value of the specific gravity γ_r:

$$\sigma_r = \sigma_e \gamma_r. \quad (4)$$

a)

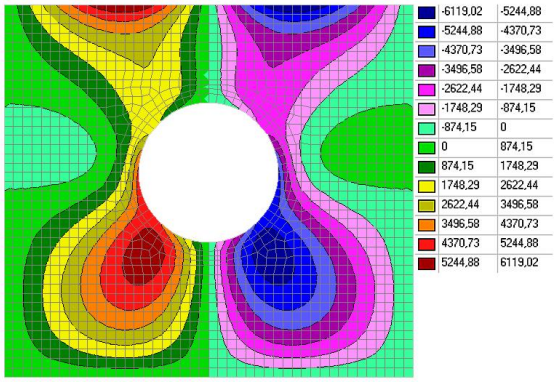

b)

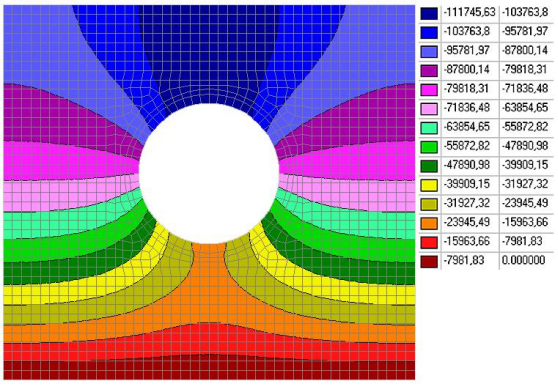

Figure 5. *The strained state of the finite-element model with unit parameters: a) displacement along the horizontal axis; b) displacement along the vertical axis*

To check the adequacy of the distribution of the stress-strain state in the finite-element model and the obtained formulas, below are the results of the calculation of the finite-element model with the values of the real characteristics of the soil (hard clay): modulus of elasticity is of E_r=35 MPa; specific gravity is of γ_r=20 kN/m^3 (**Fig. 5-6**).

As can be seen from the above results of numerical calculations, the isolines and isofields of the stressed and deformed states are qualitatively identical, and they can be obtained quantitatively by the formulas presented above. Thus, if the displacements marked in **Fig. 3**, multiply by 20 (real specific gravity) and divide by 1 (the unit value of specific gravity) and 35 (modulus of elasticity), then the displacement values can be seen in **Fig. 5**. If the stress value in **Fig. 4** multiply by 20 (real specific gravity) and divide by 1 (the unit value of specific gravity), the stress values are received in **Fig. 6**.

In the case of a horizontal supported working, only the strained state is considered, as noted above. To check the adequacy in the distribution of displacements in finite-element models, the calculation results are given below (**Fig. 7-8**).

a)

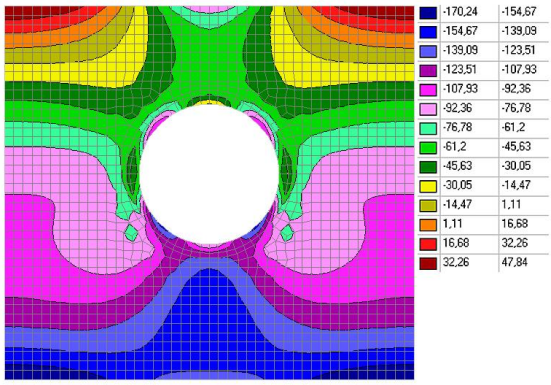

b)

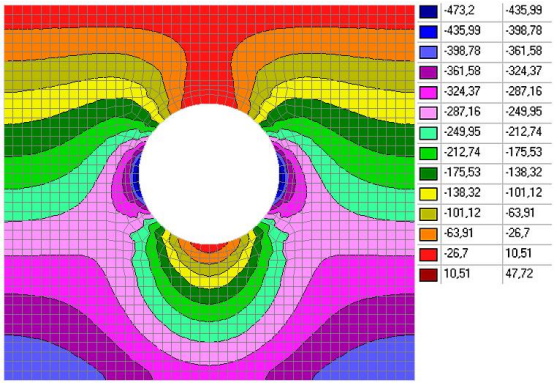

Figure 6. *The stress state of the finite-element model with unit parameters: a) stress along the horizontal axis: b) stress along the vertical axis*

Moreover, the same values of real soil characteristics are reproduced in the models of supported working as for the unsupported one.

The analysis of the components of the strained state (**Fig. 7-8**) makes it possible to conclude that the vertical and horizontal displacements are almost identical for finite-element models with a thickness of h_1=0.15 m (cast iron) and thickness of h_2=0.275 m (reinforced concrete). The error arose due to the fact that the specific gravity, which was considered during the calculation of deformations, for cast iron (72.0 kN/m^3) is almost three times more than for reinforced concrete (24.5 kN/m^3). In the case of horizontal displacements, there was also an error made by the difference between the values of Poisson's ratio (0.3 was for cast iron and 0.2 was for reinforced concrete). It is evidenced by the qualitative distribution of the horizontal component of displacements, since in the case of cast iron, the isofields are more elongated in height, in contrast to the reinforced concrete frame.

a)

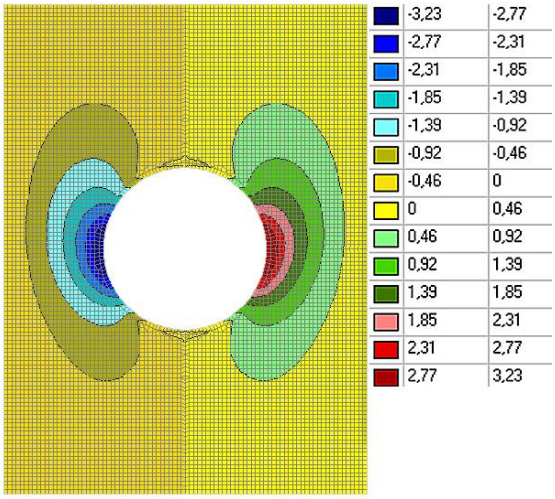

b)

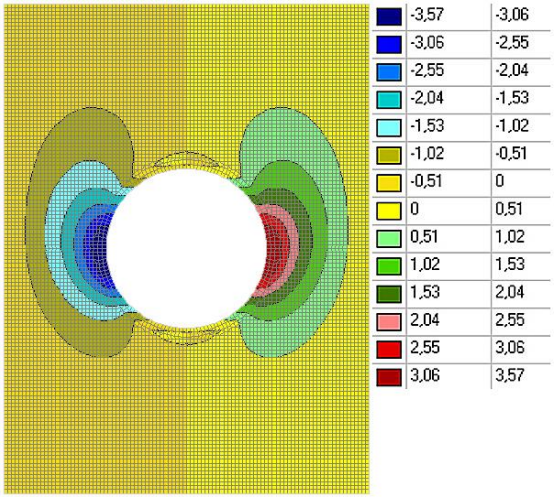

Figure 7. *The strained state of finite-element models (horizontal displacements): a) a cast iron frame with thickness of h_1=0.15 m; b) a reinforced concrete frame with thickness of h_2=0.275 m*

a)

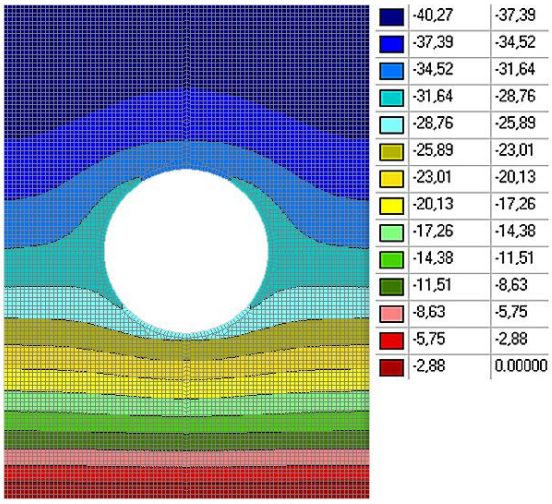

b)

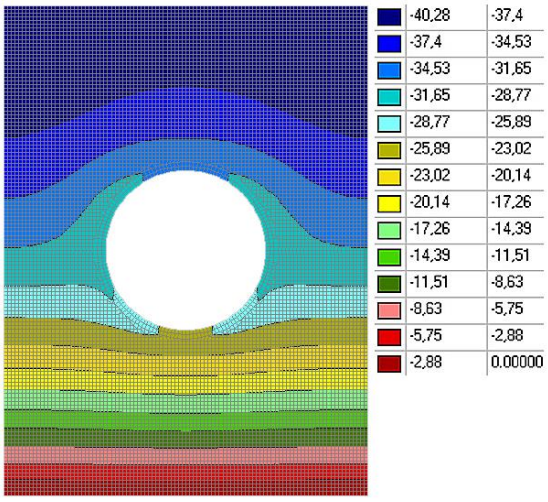

Figure 8. *The strained state of finite-element models (vertical displacements): a) a cast iron frame with thickness of h_1=0.15 m; b) a reinforced concrete frame with thickness of h_2=0.275 m*

The quantitative analysis of the values shows that for the finite-element model with a thickness of h_1=0.15 m (cast iron), the maximum horizontal displacements are 3.23 mm, the maximum vertical displacements are -40.27 mm, and for the finite-element model with a thickness of h_2=0.275 m (reinforced concrete) 3.57 mm and 40.28 mm, respectively (**Fig. 7-8**). The error values (9.5% for horizontal movements and 0.03% for vertical movements) are not significant, and it can be stated that the author's hypothesis about the equality of bending stiffness is fully confirmed.

After this confirmation, a new hypothesis can be introduced that if the equality $E_1I_1 = E_2I_2$ exists, then the expression $E_1I_1 = E_2I_2 = E_eI_e$ has to also be existed, where E_e and I_e – respectively, some values of the modulus of elasticity and the moment of inertia are equivalent and do not tie to specific materials and sections. This hypothesis makes it possible to create a finite-element model with unit parameters (a thickness is of h_e=0.1 m, and the width is of b_e=1.0 m) of the frame and, by choosing the equivalent modulus of elasticity E_e, to obtain a strained state, which is identical, for example, for the cast iron tubing frame having an open box section. For this, equation (1) should be solved accordingly for the equivalent modulus of elasticity:

$$E_e = \frac{12\ E_1 I_1}{h_e}, \tag{5}$$

$$E_e = \frac{12\ E_2 I_2}{h_e}. \tag{6}$$

The resulting formulas implement the search for the equivalent modulus of elasticity E_e both based on the modulus of elasticity for the cast iron E_1, and based on the modulus of elasticity for the reinforced concrete E_2.

IV. CONCLUSIONS

The following provisions are conclusions of the performed research of the stress-strain state for unsupported and supported horizontal underground workings.

1. Analysis of the research directions for the stress-strain state of horizontal workings based on the analytical approach and numerical methods, in particular the finite element method, demonstrates that some methodological techniques of the analytical approach can be applied during numerical analysis. After rethinking the analytical approach, the conceptual approach of Kolosov-Mushkelishvili's theory was applied to the author's constructions of parametric analysis for models with unit parameters.

2. The developed system of the parametric analysis proved that to determine the stress-strain state of horizontal unsupported workings of a certain diameter, it is enough to perform one numerical calculation of a finite-element model with unit parameters, and using simple analytical formulas, extrapolate the stress-strain state of this model to all possible cases of real workings.

3. A method of parametric analysis of the strained state of a supported working by using models with equivalent bending stiffness has been developed and substantiated. On its basis, it is possible to perform a numerical analysis of a finite-element model with unit parameters of the frame, selecting the equivalent modulus of elasticity. Thus, the results of the strained state of this model can be extrapolated to models with other geometric parameters of the frame and the material's modulus of elasticity.

ACKNOWLEDGEMENT

The publishing of this paper was supported by the Ukrainian State University of Science and Technologies.

AUTHOR CONTRIBUTIONS

O. Tiutkin: Conceptualization, Supervision, Theoretical analysis, Writing, Editing.

N. Bondarenko: Finite element modelling, Theoretical analysis, Review, Writing.

DISCLOSURE STATEMENT

The authors declare that they have no known competing financial interests or personal relationships that could have appeared to influence the work reported in this paper.

ORCID

O. Tiutkin http://orcid.org/0000-0003-4921-4758

N. Bondarenko http://orcid.org/0000-0003-0804-7500

REFERENCES

[1] D. Kolymbas, Tunnelling and tunnel mechanics, Springer-Verlag Berlin Heidelberg, 2005.

[2] S. J. Singh, Static deformation of a multilayered half-space by internal sources, Journal of Geophysical Research 75 (1970) pp. 3257–3263. https://doi.org/10.1029/JB075i017p03257

[3] M. R. Migliazza, M. Chiorboli, G. P. Giani, Comparison of analytical method, 3D finite element model with experimental subsidence measurements resulting from the extension of the Milan underground, Computers and Geotechnics 36 (1–2) (2009) pp. 113–124. https://doi.org/10.1016/j.compgeo.2008.03.005

[4] A. Hefny, H. Chua, An investigation into the behavior of jointed tunnel lining, Tunnelling and Underground Space Technology 21(3–4) (2006) p. 428. https://doi.org/10.1016/j.tust.2005.12.070

[5] D. G. G. de Oliveira, M. Thewes et al., EPB tunnelling through clay-sand mixed soils: Proposed methodology for clogging evaluation, Geomechanics and Tunnelling, 11 (4) (2018) pp. 375–387. https://doi.org/10.1002/geot.201800009

[6] V. D. Petrenko, V. T. Huzchenko et al., Analysis of deformed state structures of the Kyiv metro running tunnels on a transition zone from spondylov's clay to buchatskiy sands, Science and Transport Progress 4 (52) (2014) pp. 127–138. https://doi.org/10.15802/stp2014/27321

[7] A. R. Selby, Surface Movements Caused by Tunnelling in Two-layer Soil, Geological Society, London, Engineering Geology Special Publications 5 (1988) pp. 71–77. https://doi.org/10.1144/GSL.ENG.1988.005.01.05

[8] N. Do, D. Dias et al., 2D Tunnel Numerical Investigation: The Influence of the Simplified Excavation Method on Tunnel Behaviour, Geotechnical and Geological Engineering 32 (2014) pp. 43–58. https://doi.org/10.1007/s10706-013-9690-y

[9] M. Karakus, Appraising the methods accounting for 3D tunnelling effects in 2D plane strain FE analysis, Tunnelling and Underground Space Technology 22 (1) (2007) pp. 47–56. https://doi.org/10.1016/j.tust.2006.01.004

[10] A. Alkhdour, A. Radkevych et al., Prediction of the stress-strain state of circular workings in a layered massif by scaling, E3S Web of Conferences 168 (2020) 00020. https://doi.org/10.1051/e3sconf/202016800020

[11] A. Alkhdour, A. Radkevych et al., The parametric analysis of the supported circular working interacting with the layered massif, IOP Conference Series: Earth and Environmental Science 970 (2022) 012033. https://doi.org/10.1088/1755-1315/970/1/012033

[12] O. M. Shashenko, S. M. Hapieiev et al., Analysis of calculation models while solving geomechanical problems in elastic approach, Scientific Bulletin of National Mining University 1 (169) (2019) pp. 28–36. https://doi.org/10.29202/nvngu/2019-1/21

ACTA TECHNICA JAURINENSIS
Vol. 15, No. 4, pp. 207-220, 2022
10.14513/actatechjaur.00672

Numerical Investigation of the Effect Dimensions of Rectangular Sedimentation Tanks on Its Hydraulic Efficiency Using Flow-3D Software

Mohammad Javadi Rad[1,*], Fatemeh Rostami[2], Pedram Eshaghieh Firoozabadi[2]

[1]Department of Civil Engineering, University of Qom
Ghadir Blvd., Qom, 3716146611 Iran
[2]Department of Civil Engineering, North Tehran Branch, University of Islamic Azad
No 159, 7th Boostan St., Pasdaran Ave. North Tehran, Iran
*javadirad.mohammad@email.com

Submitted: 10/07/2022 Accepted: 14/11/2022 Published online: 18/11/2022

Abstract: Settling basins are among the essential units built to separate sediment suspended and within the inlet flow particles in water and wastewater treatment plants and irrigation canals. These basins' high efficiency requires proper design, creating a smooth and uniform flow along the basin, and reducing circulation zone as a factor in disrupting the sedimentation process. The present study investigates basin dimensions' effect on its flow pattern. Hence In the current study, the primary rectangular sedimentation basin was modelled three-dimensionally using Flow-3D software. This software takes advantage of two new advanced technique of VOF and FAVOR to model the free surface of the flow and the geometry, respectively. The dimensions of the basin were examined in two scenarios. In the first set-up, the length-to-width ratio was evaluated by increasing length and decreasing width simultaneously and the second part examined the length to depth ratio by decreasing depth and increasing width. In both situations, the volume and location of the inlet and outlet of the basin were constant and unchanged. The outcomes indicate that increasing the ratio of length-to-width and length to depth reduces the volume of the circulation zone significantly. The volume of these zones decreased from 53% for the L/W ratio of one (square basin) to 22% associated with the L/W ratio of eight. Likewise, the volume of these zones decreased by 38% as a result of increasing the L/d ratio from five to ten.

Keywords: Numerical Investigation; Rectangular Settling Tanks; Basins Dimensions; Length/Width; Length /depth.

I. INTRODUCTION

Wastewater treatment methods were originally developed for concerns about public health and environmental conditions. Since surface water is one of the important sources of water supply in different countries, research on sedimentation basins has a long history. Sedimentation tanks are responsible for the deposition of suspended particles using gravity. Because sedimentation tanks are part of the primary stages of treatment, their performance affects the efficiency of other treatment plant units. By entering the stream into the tank and reducing the flow velocity, it is possible to settle suspended particles denser than water [1]. Due to the high construction and maintenance costs of these basins, their optimal performance of them is crucial. Despite the importance of settling basins as one of the main units of treatment plants, the existing design methods rely heavily on the empirical formulas of researchers who need to consider the hydrodynamic details of flow and sediment fully.

Where the sedimentation tank is efficiently designed and operated, the suspended solids decrease by about two-thirds. Generally, these tanks are designed to provide a hydraulic retention time of about 1.5 to 2.5 hours based on the average flow rate [2]. Primary sedimentation tanks are designed based on the surface load, while secondary sedimentation basins are designed according to the surface and solid load. Influential factors in the sedimentation process include surface load, basin shape and depth.

Circulation zones are one of the most common adverse factors in sedimentation basins. These zones create by short-circuiting between the inlet and outlet of the tank, which resulted in dead zone development and optimal sedimentation reduction. Reducing the dead zones inside the tank provides a suitable potential for sedimentation. As the size of the sedimentation tanks increases, the loading capacity and, consequently the effective level of sedimentation increase. However, this requires large costs in its construction, operation, supply and maintenance. Therefore, the use of alternative methods to optimize performance and increase the efficiency of the sedimentation tank feat the existing conditions is necessary and inevitable.

Kawamura (2000) [3] concluded that many factors in water and wastewater treatment would affect the performance of the sedimentation tank. The four types of effects that were not considered until then are:

- Basin geometry, such as its structure, location and arrangement of inlet and outlet.
- Flow characteristics such as density effects may make the velocity profile uneven. This effect may cause a short circuit from the inlet to the outlet, re-sedimentation of sediment particles and increased turbulence intensity.
- Particle removal systems may disturb the flow's stability and uniformity.
- Environmental and climatic aspects, such as air, wind gap and internal temperature of the stream.

Razmi et al. (2008) [4] bridged the gap of experimental data and carried out a serious lab test using the Acoustic Doppler Velocimeter (ADV), which measures instantaneous speed in three directions. In addition to the non-baffle test, they examined the baffle's effect on the flow's hydrodynamics. Their results show that:

- The presence of a baffle in the primary zone is more effective than in the middle zone.
- The optimal location of the baffle is the point where the volume of the circulation zone of the fluid inside the basin is minimal.

Rostami et al. (2011) [5] simulated the flow characteristics in the primary sedimentation basin using a computational fluid dynamics model. In this modelling, an incompressible and non-floating liquid is assumed. Besides, a turbulent RNG model with Navier-Stokes equations is used. In order to investigate the hydraulic effects on the velocity profile, separation length, and kinetic energy, three different input positions and three baffles at the input have been simulated. In this model, the fluid flow moves through the network, and the free surfaces are tracked by the liquid volume (VOF) method. The effects of the number and locations of the input baffle in the flow field are shown. The results indicate that the input baffle's position affects the sedimentation basin's flow pattern. An increase in fissures and inlets can reduce kinetic energy in the input area and cause a uniform flow. Shahrokhi (2012) [6] investigated the reduction of kinetic energy in a 2-meter length laboratory sedimentation tank based on flow patterns. In this research, the tank's number and position of flow inputs have been investigated to increase productivity and efficiency. From the results, it has been observed that two inputs in the middle (relative to the height) and at the same distance (relative to the symmetry line of the basin) produce the highest efficiency according to the flow patterns.

Patziger (2016) [7] aimed to improve shallow circular secondary basins (SSTs) using numerical fluid dynamics (CFD) analysis and observed a direct relationship between inlet height and inlet jet radial length in shallow circular secondary basins. To calculate and evaluate the performance of the basin, Lee (2017) [8] investigated the effect of double perforated baffle on solids removal in rectangular secondary basins using CFD simulations. It was observed that the double-perforated baffle impedes longitudinal movement and reduces the density of suspended sediments in the wastewater. He also recommended the installation of this baffle in rectangular secondary basins to reduce the total operating costs of wastewater treatment plants. Liu (2017) [9] performed a numerical simulation of the effect of the baffle on the hydraulic properties of the flow and the particle removal efficiency from a sedimentation basin by combining two liquid and solid phases using $k-\varepsilon$ turbulence model. The length of their modeled basin was about 21 meters. Their results showed that with the horizontal distance of the baffle between 0.5 to 2.5 meters from the input, the amount of particle removal increases. Also, with increasing the submerged depth of the baffle from 0.5 to 2 meters and especially with increasing it from 0.5 meters to one meter, the amount of particle removal obviously increases.

Zanganeh et al. (2017) [10] in a laboratory model showed that the possibility of increasing the efficiency of primary sedimentation tanks by using thin layer plates will cause more sedimentation of suspended solids. Increasing the productivity of sedimentation tanks in the wastewater treatment plant is important for technical and economic reasons, so finding a model to increase the

productivity of sedimentation tanks is necessary and essential. This study, which uses thin-film plates of minerals in the sedimentation tank, in the laboratory and using a mathematical model, actually compares the efficiency of the actual volume of the tank equipped using thin-layer plates in the laboratory model with the tank under normal conditions (without using thin layer plates). The results depict that the velocity in the tanks equipped with thin-layer plates of minerals was 1.6 m/s less than the tank in normal conditions.

Javadi Rad et al. (2017) [11] conducted research on the number of baffle structures in the actual sedimentation basin of the southern Tehran wastewater treatment plant. Based on the conformity of the numerical results with the experimental data, the $k-\varepsilon$ turbulence model was used to solve the flow turbulence, therefore the appropriate accuracy of the numerical results was assured. The optimal location of the first baffle was determined from the authors' previous research. To determine the optimal number of baffles, the results were compared between tank without baffles and optimal conditions of tank with one, two and three baffles. The outcomes reveal that the presence of baffle structure prevents the flow jet in the floor and hence increases the deposition efficiency of the initial sedimentation basins. In addition, by adding a baffle in the right position, the magnitude of the maximum speed, the volume of the circulation zone and the kinetic energy are reduced, so that by adding the first, second and third baffles the volume of the circulation zone decreases by 4.13, 4.44 and 4.63% respectively. Zhou et al. (2018) [12] adopted a three-dimensional model to evaluate the performance of a long rectangular secondary basin. The results of simulations showed that one baffle and two perforated baffles in a row have the best performance. The predicted results of the model are well matched with field observations.

Aminnejad and Lajevardi (2018), [13] investigated the effect of basin shape on the amount of sediment. For this purpose, he has considered sedimentation ponds with normal urban dimensions and conditions and has studied the flow field and sediment density in the basins using multiphase flows and numerical methods as well as Fluent software. Then, changes were made in its dimensions in terms of length, width and height with a fixed volume and its effect on efficiency was investigated. The results of calculations showed that contrary to previous researchers who considered the length of the basin as the most effective parameter in sedimentation, due to the coarseness of particles and geometric properties of urban basins, increasing the width of the pond in the direction perpendicular to the flow axis has the highest effect.

Alighardashi and Goodarzi (2019) [14] studied the hydraulic efficiency of sedimentation tanks. In that paper, they aim to investigate the effects of the depth and wind on the water's surface on the hydraulic efficiency of the sedimentation tanks in water and wastewater treatment plants. A verified two-dimensional numerical study was performed to evaluate the hydraulic performance of series settling tanks by four different depths of 2.5, 3, 3.5 and 4 (m) and wind velocities of 5 and 7 (m/s). In both rhetorical and typical situations, the Real Hydraulic Retention Time and the adequate volume of sedimentation tanks increase widely as the tank depth.

Bouisfi et al. (2019) [15] researched improving the removal efficiency of sedimentation tanks using different inlet and outlet positions using the Computational Fluid Dynamics method. Two different configurations have been proposed and tested with varying particle diameters and concentrations. The numerical model's ability to describe flow field behaviour inside the tank is confirmed by experimentation data. Results show that inlet and outlet position influence the flow field and removal efficiency of sedimentation tanks, especially in the case of fine particles (50 and 120μm).

Patel et al. (2021) [16] simulated a rectangular and circular primary clarifier. The modelling of clarifiers is carried out using one-dimensional flux theory or two-dimensional computational fluid dynamics. The experiments were performed for three operating conditions, i.e. high, medium and low solid concentrations, using a lab-scale setup. The one-dimensional sedimentation process model was carried out on the MATLAB platform, and simulation was carried out. Based on the simulation and experimental outcomes, the removal of suspended solids is found to be better in circular clarifiers compared to rectangular clarifiers for an influent flow rate of 134 mL/min with influent total suspended solids ranged from 300 to 600 mg/L.

In the present study, the length/width (L/W) and length/depth (L/d) ratio of the sedimentation basin dimensions is investigated. Due to the relatively large occupied area and the construction costs of rectangular basins, its dimensions are of great importance. In these basins, the flow is horizontally in the direction of the basin. The length-to-width ratio of these basins is usually between 2 and 5 and sometimes up to 7. The higher this ratio, the less

likely it is that a short circuit will occur between the input and output. Monk [17] considered the L/W ratio of 6 to 7 to be appropriate due to the short circuit control. Research on the dimensions of the basin has rarely been done and most of them has been done to improve the performance of the basin by making baffles in the flow path. This indicates the need for research on the dimensions of tanks.

In past research, the ratios of length-to-depth and length-to-width were not investigated simultaneously, and the available data needed more for comparison. Also, a time gap was observed in the research related to the geometric survey of rectangular tanks.

The limitations of this research are associated with its laboratory dimensions and the fact that the flow is not affected by the concentration of materials. Of course, in primary sedimentation tanks, due to the concentration lower than 200 mg/litre (Stamo, 1989), the flow is rarely affected by the concentration of materials. Also, the input flow to the tank is assumed to be uniform [18].

An introduction to existing research and a review of past research were described. In the following sections, the equations governing the flow using the fluid volume of the fractional areas and the method used in the research, the preparation of the models and the description of the boundary conditions and the structure of the mesh and the verification of the numerical models and finally the discussion of the results and conclusions It is described.

Figure 1. *Rectangular settling basin*

II. FLOW GOVERNING EQUATIONS

The equations governing Newtonian incompressible fluid flow encompass the continuity equation and the momentum equations in three main directions. The most important law used in the movement of fluids and in the water flow is the law of conservation of mass. From this law and using the mass equilibrium relationship at the input and output for a very small fluid element, the continuity equation can result. The continuity equation for this element is as follows [19]:

$$\frac{\partial \rho}{\partial t} + \nabla.(\rho V) = 0 \tag{1}$$

Which results in:

$$V_f \frac{\partial \rho}{\partial t} + \frac{\partial}{\partial x}(\rho u A_x) + \frac{\partial}{\partial x}(\rho v A_y) + \frac{\partial}{\partial x}(\rho w A_z) = 0 \tag{2}$$

Where, ρ and V_f are flow density and deduction of open volume to flow respectively. u, v and w are also velocities of the flow in the principal directions x, y and z respectively.

After applying the continuity equation, the principle of motion size conservation or momentum in fluid motion must also be considered. The Navier–Stokes equations are the equations governing the motion of a viscous Newtonian flow with velocity components in the three principal directions x, y, and z as follows [6]:

$$\frac{\partial u}{\partial t} + \frac{1}{V_f}\left\{uA_x\frac{\partial u}{\partial x} + vA_y\frac{\partial u}{\partial y} + wA_z\frac{\partial u}{\partial z}\right\} = -\frac{1}{\rho}\frac{\partial \rho}{\partial x} + G_X + f_x \tag{3-a}$$

$$\frac{\partial v}{\partial t} + \frac{1}{V_f}\left\{uA_x\frac{\partial v}{\partial x} + vA_y\frac{\partial v}{\partial y} + wA_z\frac{\partial v}{\partial z}\right\} = -\frac{1}{\rho}\frac{\partial \rho}{\partial y} + G_y + f_y \tag{3-b}$$

$$\frac{\partial w}{\partial t} + \frac{1}{V_f}\left\{uA_x\frac{\partial w}{\partial x} + vA_y\frac{\partial w}{\partial y} + wA_z\frac{\partial w}{\partial z}\right\} = -\frac{1}{\rho}\frac{\partial \rho}{\partial z} + G_z + f_z \tag{3-c}$$

Where G_X, G_y and G_z are acceleration of mass gravity and f_x, f_y and f_z are accelerations of viscosity.

III. RESEARCH METHODS

Nowadays numerical methods are very popular since they are fast, inexpensive and also eliminate limitations of analytical and experimental methods. In numerical methods, differential equations are numerically integrated at different times and places. In summary, in numerical methods for solving differential equations, the networking range is first determined and using time and space discretization methods, the differential equations are transformed into simple and solvable algebraic equations. Computers solve the resulting numerical equations on all defined network points or finite volumes, the accuracy of which depends on the discretization method used. Due to the repetition of the solution in different time and space periods and the high volume

of calculations, the accumulation of errors in these methods is possible.

Flow-3D software has been considered as one of the newest, most popular and powerful software for numerical solution of three-dimensional motion of fluids. Although this software has been used for modelling all fluids, due to its special features it is especially used in hydraulic problems and has provided highly acceptable answers in this field. Thanks to a powerful graphical user interface which makes Flow-3D a user-friendly software [20].

This software takes advantage of two new advanced technique of VOF and FAVOR to model the free surface of the flow and the geometry, respectively. These models include: Prantel mixing length, single equation transfer model, two equation model of $k-\varepsilon$, two equation RNG model, LES large vortex simulation model, which shows the possibility of modelling a wide range of turbulent flows using Flow–3D.

Flow-3D software is equipped with a volume of fluid (VOF) scheme to give a more realistic analysis of the free surface flow. Cartesian, staggered grids are employed to solve the RANS equations (Reynolds Average Navier–Stokes), composed of continuity and momentum equations. [21 ,22] The VOF method consists of three main components: the definition of the VOF function, a method to solve the VOF transport equation, and the setting of boundary conditions at the free surface. Within the frame of VOF methods, the interface is determined from the volume fraction F [21]. Here, F is the fraction function. In particular, F = 0 when a cell is empty and F = 1 when a cell is full. The free surface is located at a position on intermediate values of F (the user may usually define F = 0.5, but another intermediate value) [23].

IV. SETUP MODEL

The modelled sedimentation tank includes an inlet at a height of 10 cm from the bottom of the tank and an outflow at the end. The inlet and outlet of the flow in all models is constant in the total width of the basin and the volume of the tank. It should be noted that three-dimensional geometric shape of the tank was drawn in the Flow-3D software due to its simplicity. However, in case of complex geometry, it should be drawn in software such as 3D AutoCAD and the STL output should be taken then from it and entered into Flow-3D. In this research, $k-\varepsilon$ turbulence model is used. Due to the compliance of results from the $k-\varepsilon$ turbulence model and experimental data. In addition, the acceleration in the z direction was placed at -9.81.

The main characteristic of the Flow-3D software is using a rectangular meshing system with high changeability for networking. This feature makes the network and the model geometry separate from each other. In simpler terms, it does not use a geometry-connected mesh system [24]. The blocks must either be placed exactly next to each other, which is called the linked blocks, or they must be placed completely inside each other, which are called nested blocks. The mesh is defined independently for each of the three orthogonal coordinates. Thus, numerical simulations were conducted with various numbers of cells to find the grid-independent solution. In this modelling, 225, 102 and 55 cells were used for the model length, width and height of 2, 0.5 and 0.3 m respectively. The smallest and largest dimension of a cell is about 5 and more than 10 mm respectively. **Fig. 2** demonstrates a three-dimensional view of the settling tank as well as the model grid in Flow-3D. The FAVORize tool is used to grid the model. Before starting to run the model, this tool spectacles exactly how well the software has correctly identified the model geometry (**Fig. 3**). This will assist to increase or decrease the size or number of cells if necessary.

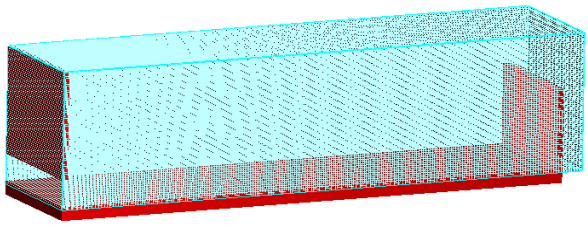

Figure 2. *A view of settling basin and its gridding drawn tree-dimensionally in Flow-3D software*

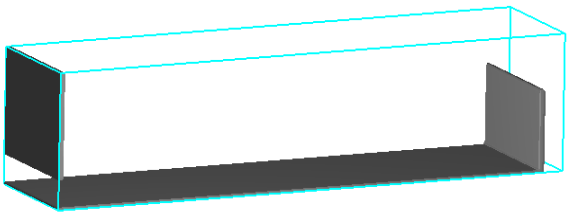

Figure 3. *Realized geometry of the model using FAVORize tool*

Input boundary condition: In order to determine unknown variables such as speed and pressure the input boundary condition should be defined in the model. Using the “Specified Velocity” option, the input velocity was defined as 0.04 m/s for all models.

Output boundary condition: By selecting the “Outflow” option for the output part after the overflow, the flow leaves the model horizontally.

Basin floor and wall boundary condition: Flow-3D with the power of the FAVOR method detects walls and floor, but the Wall option is selected for basin floor and walls. Due to the tank dimensions and the existence of a rigid boundary on both sides and its floor, the condition of zero velocity and no change of other parameters are applied by applying the boundary condition.

Boundary condition of flow-free surface: Flow-3D software uses the VOF method to solve free surfaces that simulate water and air boundary conditions as fluid volume. The boundary condition for the upper face in the vicinity of the air in the sediment tank is the "Symmetry" option; the symmetry condition is applied for zero gradient perpendicular to the boundary. The velocity and pressure changes in this boundary are zero to infinity. **Fig. 4** addresses the designated boundary conditions.

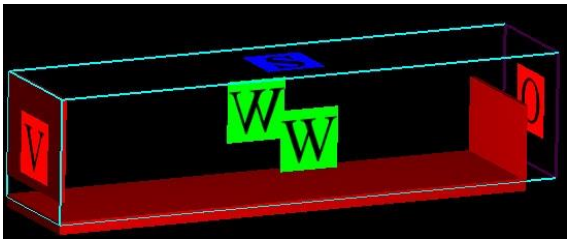

Figure 4. *A picture of the boundary conditions set for the study model*

In the current study the version of 11.2 of Flow-3D was used. All the numerical options were taken as the default value of the Flow-3D software. For example: The GMRES solver is a new algorithm in Flow-3D that was used in this numerical model. The GMRES pressure solver possesses good convergence, symmetry, and speed properties. However, it uses more memory than the SOR or the SADI methods.

The important topic in this research is the last two columns of **Table 2** including the length-to-width ratio and the length to depth ratio in a fixed volume of 0.3 m^3. Case No. 3, which is the same as the physical model constructed in Shahrokhi et al. lab, is the basic model of current study that is used in both scenarios of L/W and L/d ratio. To compare the L/W ratio, the results of cases 1, 2, 3 and 4 are used while for L/d ratio the outcomes of cases 3, 5 and 6 are evaluated.

V. VERIFICATION TEST

In order to verify the results of numerical modelling of the sedimentation tank, the numerical results were compared with the experimental data of Shahrokhi et al. The dimensions of their rectangular primary settling tank included a length (L) of 200 cm, a width (W) of 50 cm, a water depth (H) of 31 cm, an inlet opening height (H_{in}) of 10 cm, and an outlet weir height (H_w) of 30 cm.

The numerical results show good agreement with experimental data (**Fig. 5**), but some errors are observed near the bed, specifically in the regions near the inlet zone. The discrepancies between the result of the computational model and experimental measurements are probably due to the differences of the flow patterns in the inlet section. Also, **Table 1** shows the measured values root mean square errors (RMSE) of velocity profiles of experimental data and numerical results.

VI. RESULTS AND DISCUSSION

Based on the models addressed in **Table 2**, the results obtained by comparing the different dimensions of the rectangular basin are presented and reviewed. This section is described in two parts: L/W and L/d ratio. As previously mentioned, in all models, the volume of the tank is fixed and the inlet and outlet locations are unchanged. Besides, the inlet and outlet cover the entire width of the tank.

1. Comparison of L/W ratio of settling tank

In this section, considering fixed depth and volume equal to 0.3 m and 0.3 m^3, respectively, with simultaneous changes in the length and width of the tank, four different cases named 1, 2, 3 and 4 were raised whose dimensions are reported in **Table 2**.

Fig. 6 displays the streamlines and circulation zone for cases 1 to 4 in different length-to-width ratios. Cases 1 to 4 have L/W ratios of 1, 2, 4 and 8, respectively. It is observed that with increasing the L/W ratio (increasing the length and decreasing the width simultaneously) the volume of the circulation zone has decreased. In **Fig. 6 (a)** which is associated with the model with a length-to-width ratio of one (square tank), the volume of the circulation zone is calculated as equal to 53% of the total volume of the tank. While with the increase of length /width ratio, this volume has reached 22% in case number 4. The volume of circulation zone all four models is given in **Table 3**.

Fig. 7 depicts the kinetic energy contours for cases 1 to 4 with different length-to-width ratios. The length of the maximum kinetic energy (red zone) prevents proper particle sedimentation. This zone represents the flow jet after the inlet, therefore the shorter this zone the sedimentation performance the higher. Fig. 6-a shows that this zone covers about 80% of the length of the tank. By increasing the length-to-width ratio, the length of the zone with the maximum kinetic energy decreases, so that in case number 4, the length of this zone has reached less than 30% of the length of the sedimentation tank.

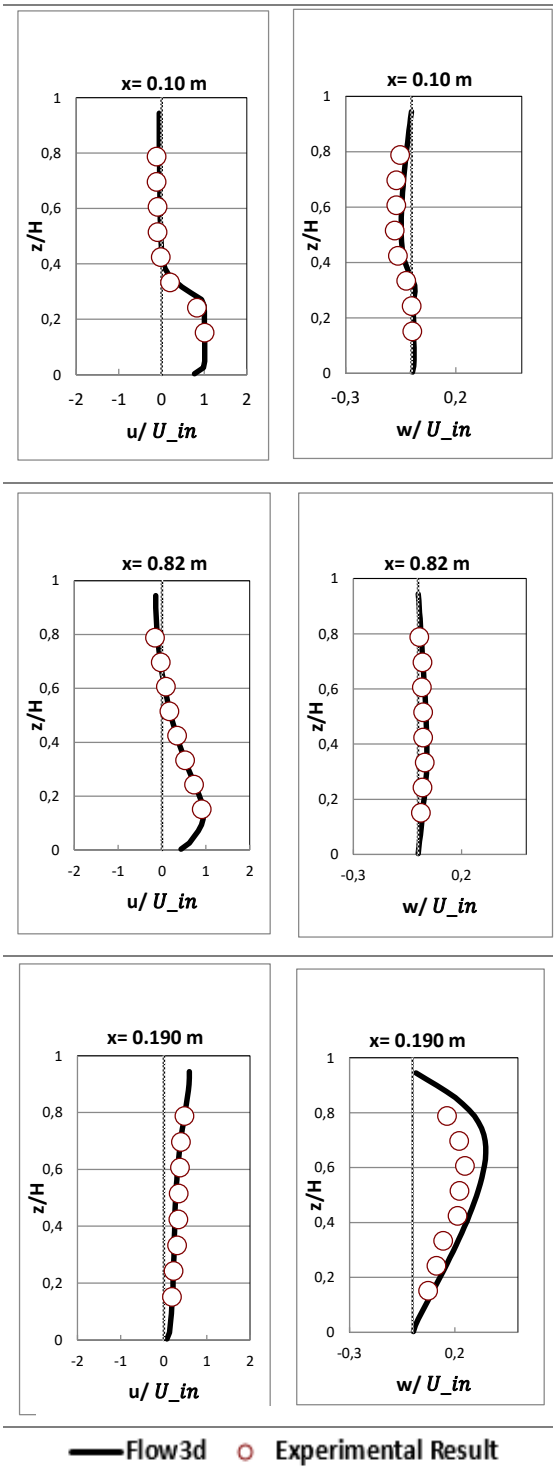

Figure 5. *Comparison between experimental and computational x-velocity and z-velocity component (z is transverse distance from the bed and u_{in} is inlet velocity)*

Table 1. *The measured values root mean square errors of velocity profiles of experimental data and numerical results*

Distance from the inlet (cm)	**10**	**82**	**190**
RMSE (in the x-direction)	0.11	0.07	0.08
RMSE (in the z-direction)	0.13	0.10	0.19

2. Comparison of basin L/d ratio

In the second part of the results, the ratio of L/d of the rectangular basin is evaluated. In this survey, the volume of the tank is fixed at $0.3\,m^3$ same as previous sub-section but this time the length of the tank has a fixed amount of 2 m and the width and depth are changing. Cases 5, 3 and 6 with the length-to-depth ratio of 5, 7 and 10, respectively are compared. Other specifications of the models are given in **Table 2**. Depth in the mentioned models is 0.4, 0.3 and 0.2 meters, respectively.

Fig. 8 demonstrates the streamlines from the inlet to the outlet within the basin. It is shown that by increasing the ratio of L/d (decreasing the basin depth), the volume of the circulation zones decreases. Circulation zones prevent sedimentation by creating transverse and sometimes reversible velocities. The minimum volume of the circulation zone is associated with case number 6 (with the maximum L/d ratio) by 16% of the total volume of the tank. Furthermore, an increase in the length-to-depth ratio results in a decline in the circulation zone length, which improves the performance of the tank. **Table 4** shows the circulation zones volume for models as a percentage of the total tank volume. However, case No. 6 with the highest length-to-depth ratio has the lowest circulation zone.

Table 2. *Dimensions of simulated models of settling basin (all units are in meter)*

case number	***Length***	***Width***	***Depth***	***L/w***	***L/d***
1	1	1	0.3	1	7
2	1.4	0.700	0.3	2	7
3	2	0.500	0.3	4	7
4	4	0.250	0.3	8	7
5	2	0.375	0.4	4	5
6	2	0.750	0.2	4	10

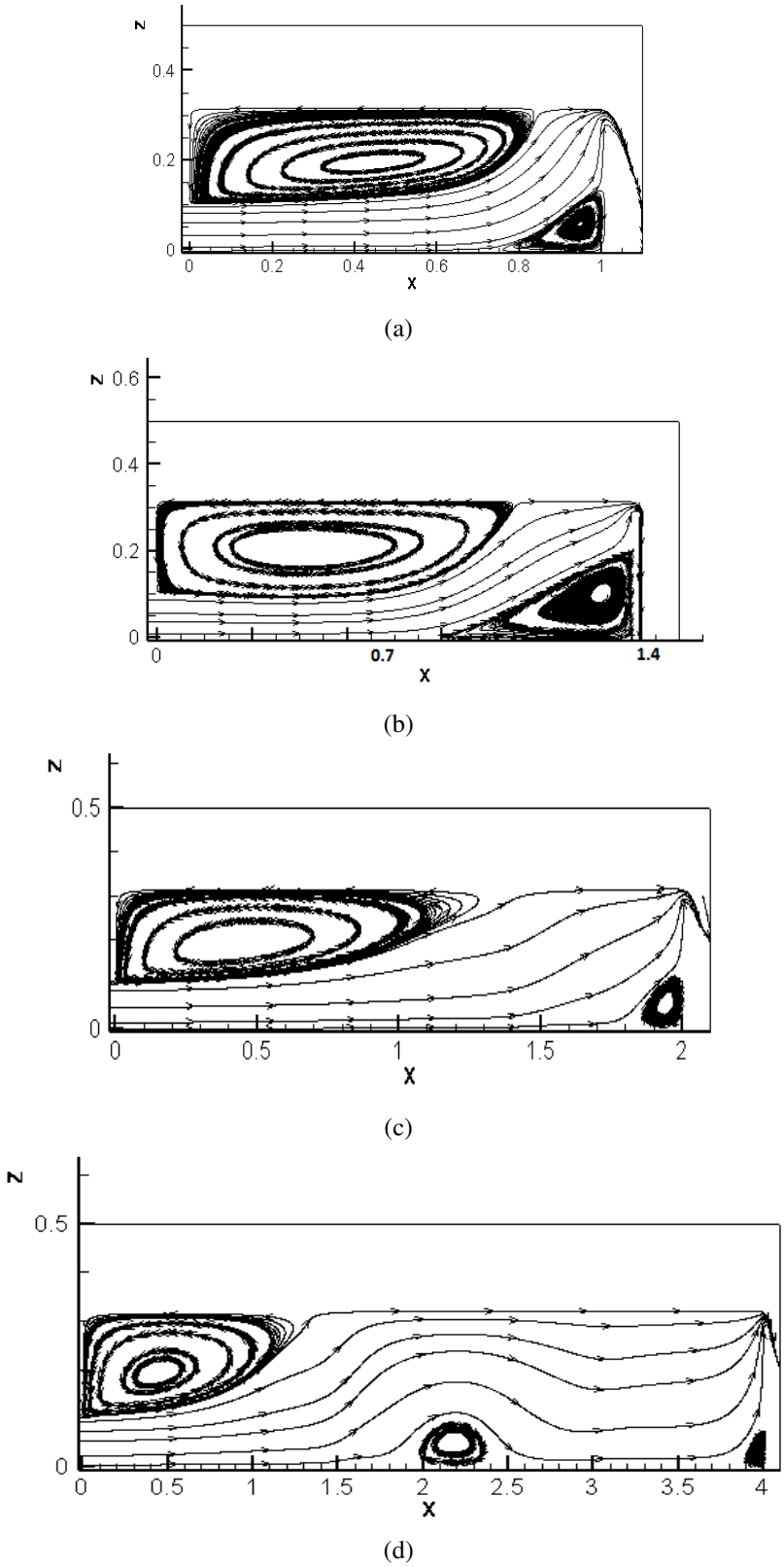

Figure 6. *Comparing the streamlines and circulation zone volume of rectangular basin for different L/W of: (a) case 1 (b) case 2 (c) case 3 (d) case 4*

Table 3. *Comparison of circulation zone volume for different L/W of rectangular basin.*

L/w	***1***	***2***	***4***	***8***
Circulation zone volume (%)	53	48	38	22

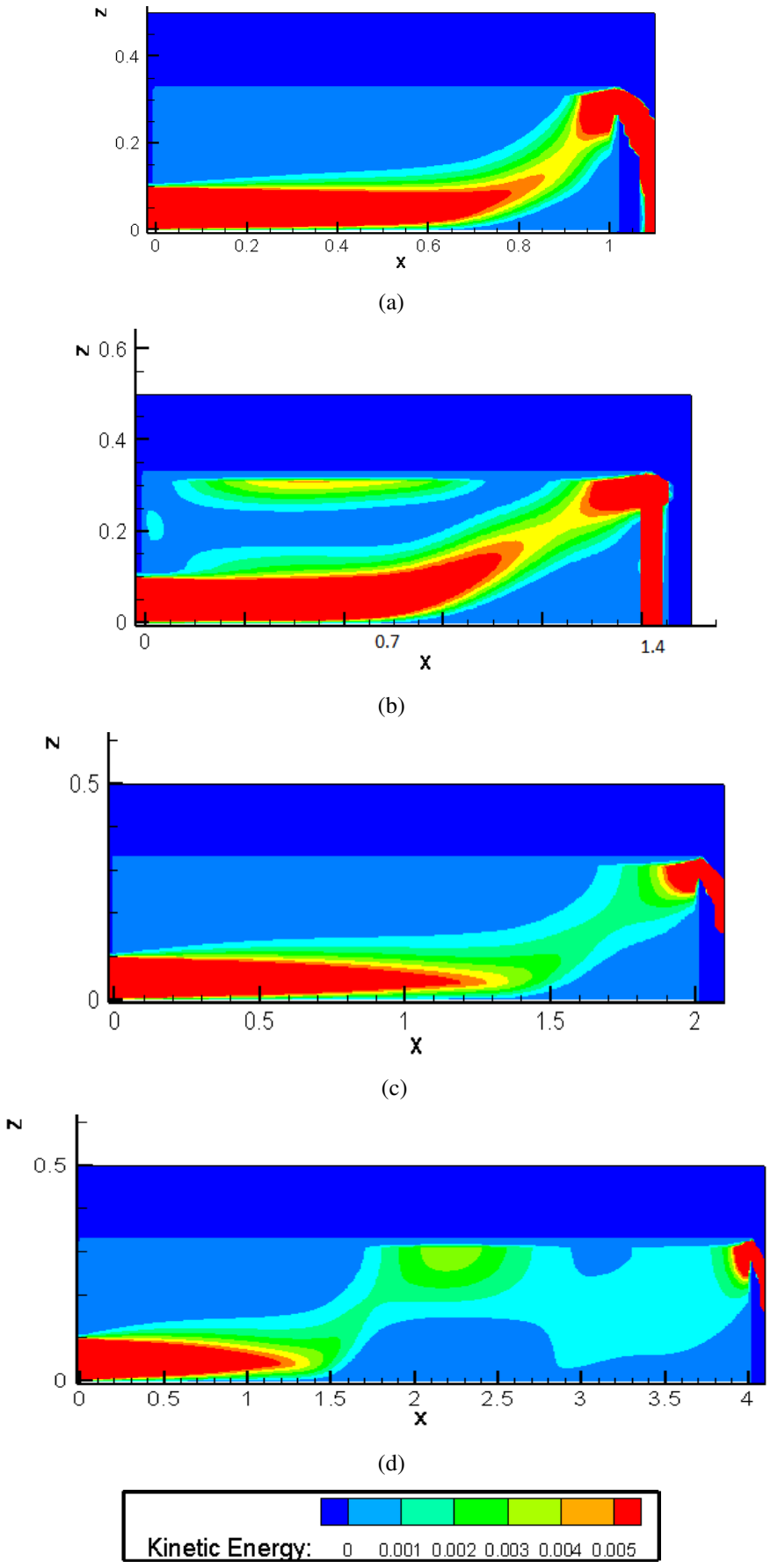

Figure 7. *Comparison of kinetic energy counters (m^2/s^2) for rectangular basin with L/W of: (a) case 1 (b) case 2 (c) case 3 (d) case 4*

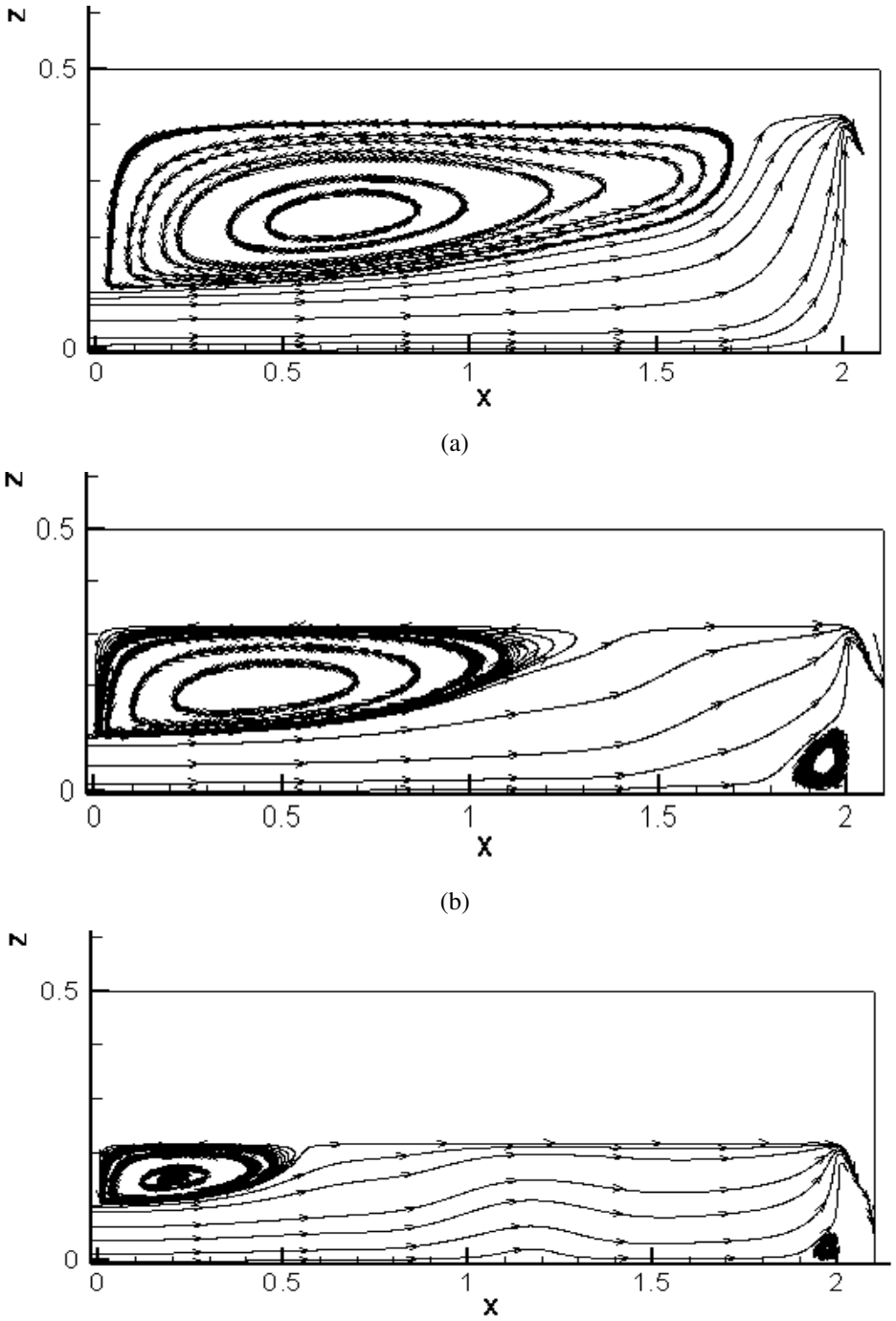

Figure 8. *Comparison of streamlines and volume of circulation zones for a rectangular basin with the L/d ratio of: (a) case 5 (b) case 3 (c) case 6*

Table 4. *Circulation zone volume for different L/W of rectangular basin.*

L/W	***5***	***7***	***10***
Circulation zone volume (%)	54	38	16

Fig. 9 compares kinetic energy contours for different models of L/d ratio. The length of the area with maximum kinetic energy for cases 5, 3 and 6 is 1.5, 1.3 and 0.9, respectively, which includes 75, 65 and 45% of the total length of the basin, respectively. The results indicated that case No. 6 with the shortest

length of the maximum kinetic energy zone has the best performance in sedimentation. Also, in **Fig. 9-c**, associated with case No. 6, the maximum kinetic energy contours have moved upwards before the middle of the tank, which causes a smooth and uniform flow near the floor and consequently improves the efficiency of the tank.

VII. CONCLUDING REMARKS

The required factor for the high efficiency of sedimentation basins is proper design and creation of a smooth and uniform flow along the basin which reduces circulation zones as an agent in disrupting the sedimentation process. In this research, the primary rectangular sedimentation basin was modelled using Flow-3D software in a three-dimensional environment. The purpose of this study was to investigate the effect of basin dimensions on the flow pattern within these basins. Hence, the present study was conducted in two scenarios. In both scenarios, the volume and location of the inlet and outlet of the basin were constant and unchanged.

The outcomes of this study reveal that by increasing the length-to-width ratio, the volume of the circulation zones decreases significantly. The volume of these areas increased from 53% for the L/W ratio of one (square basin) to 22% for the L/W ratio of 8. Besides, as the length of the basin increases and the width of the area decreases, the maximum kinetic energy also decreases. In such a way that by increasing the L/W ratio by 4 times this zone declined from 80% to about 30% of the total length of the tank. In the second part of the research, by increasing the L/d ratio of the basin from 5 to 10, the volume of circulation zones decreased from 54% of the total basin to 16%. Likewise, by increasing the L/d ratio at a depth of 0.2 m, the length of the zone with maximum energy reached 0.9 m, which is the lowest value compared to other models. In summary, for increasing the efficiency of sedimentation basins, it is suggested that the ratio of L/W and L/d adopt at least 4 and 7 respectively.

Other numerical models in the field of fluids dynamic can be used to compare with the results of this research. Also suggest to check more ratios of length to width and length to depth of basins in order to achieve more accurate dimensions. It is suggest to check the shape of the basins, for example, L-shaped tanks should be used in the research.

AUTHOR CONTRIBUTIONS

Mohammad Javadi Rad: Formal analysis, Visualization, Writing - original draft. Author: Conceptualization, Experiments, Theoretical analysis.

Fatemeh Rostami: Investigation, Resources, Visualization

Pedram Eshaghieh Firoozabadi: Supervision, Review and editing.

DISCLOSURE STATEMENT

The authors declare that they have no known competing financial interests or personal relationships that could have appeared to influence the work reported in this paper.

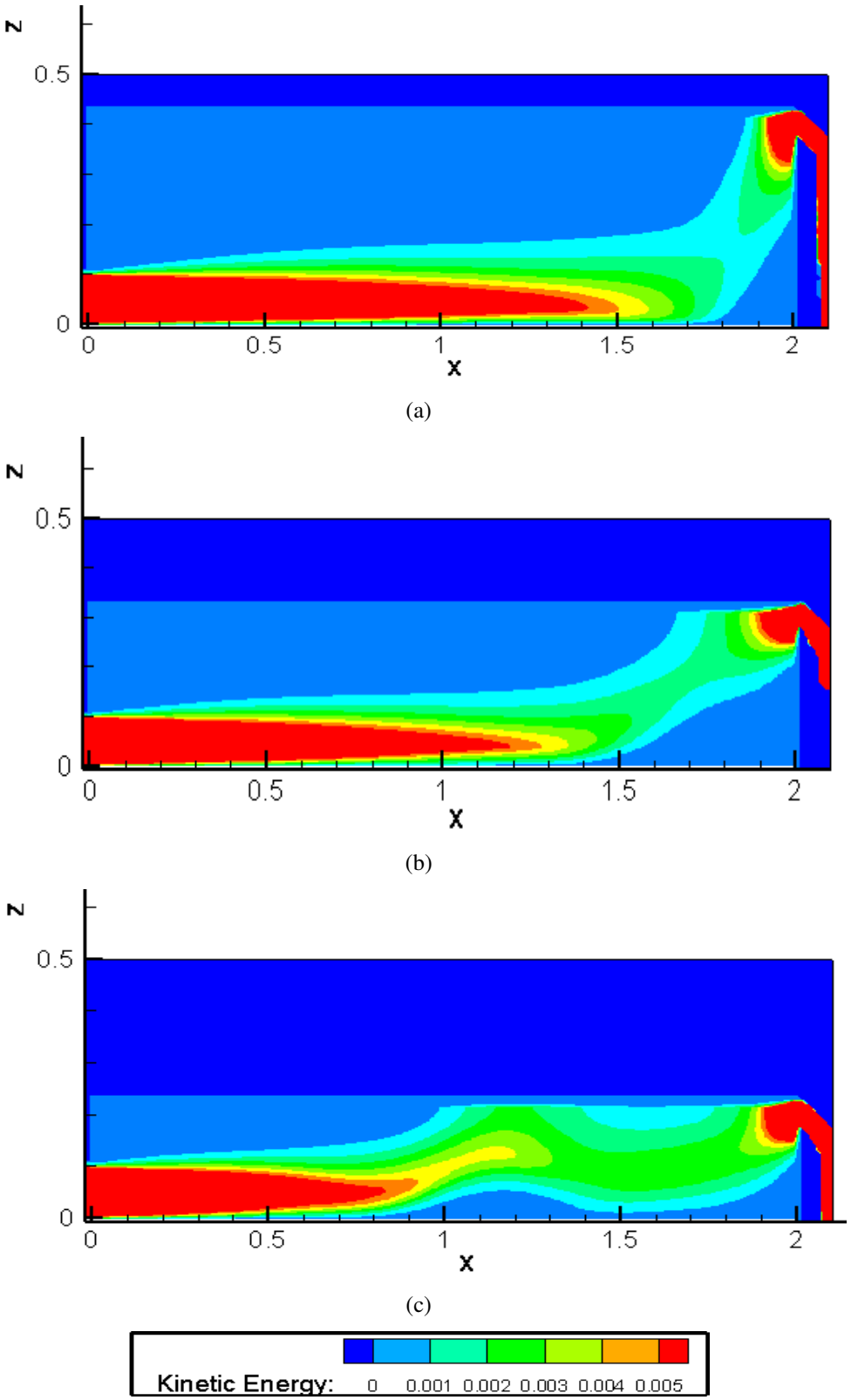

Figure 9. *Comparison of kinetic energy counters (m^2/s^2) for rectangular basin with L/W of: (a) case 5 (b) case 3 (c) case 6*

REFERENCES

[1] H. Asgharzadeh, B. Firoozabadi, H. Afshin, Experimental investigation of effects of baffle configurations on the performance of a secondary sedimentation tank, Sharif University of Technology (2011) pp. 938-949.

[2] Metcalf & Eddy 2003. Wastewater engineering treatment and reuse, New York, McGraw-Hill.

[3] S. Kawamura, Integrated design and operation of water treatment facilities, 2nd ed.; John Wiley and Sons Inc.: New York, NY, USA, (2000) pp. 159–160.

[4] A. Razmi1, B. Firoozabadi1, G. Ahmadi, Experimental and numerical approach to enlargement of performance of primary settling tanks, Journal of Applied Fluid Mechanics 2 (1) (2009) pp. 1-12.
https://doi.org/10.36884/JAFM.2.01.11850

[5] F. Rostami, M. Shahrokhi, Md Azlin Md Said, A. Rozi, Syafalni, Numerical modeling on inlet aperture effects on flow pattern in primary settling tanks, Applied Mathematical Modelling 35 (6) (2011) pp. 3012-3020.
https://doi.org/10.1016/j.apm.2010.12.007

[6] M. Shahrokhi, Influence of Baffle structure on the improvment efficiency of primary rectangular sedimentation tank, Universiti Sains Malaysia (2012) pp. 42-99.

[7] M. Patziger, Computational fluid dynamics investigation of shallow circular secondary settling tanks: inlet geometry and performance indicators, Chemical engineering research and design 112 (2016) pp. 122–131.
https://doi.org/10.1016/j.cherd.2016.06.018

[8] B. Lee**,** Evaluation of double perforated baffles installed in rectangular secondary clarifiers, (2017).

[9] Y. Liu, P. Zhang, W. Wei, Simulation of the effect of a baffle on the flow patterns and hydraulic efficiency in a sedimentation tank. Desalination and Water Treatment, 57 (54) (2016) pp.1-10.
https://doi.org/10.1080/19443994.2016.1157521

[10] H. Zanganeh, S. Narakorn, Three-dimensional VIV prediction model for a long flexible cylinder with axial dynamics and mean drag magnifications. Journal of Fluids and Structures (2016) pp. 127–146.
https://doi.org/10.1016/j.jfluidstructs.2016.07.004

[11] M. Javadi Rad, M. Shahrokhi, T. Rajaee, Numerical investigation of the number of baffles effect on the efficiency of primary sedimentation tank in true dimensions, Modares Civil Engineering Journal (M.C.E.J) 17 (5) (2017) pp. 49-59.

[12] S. Zhou, C. Vitasovic, J.A. McCorquodale, S. Lipke, M. DeNicola, P. Saurer, Improving performance of large rectangular secondary clarifier. Available online: (28 April 2017).
https://hydrosims.com/files/Optimization_Rectangular_Clarifiers.pdf

[13] B. Amin nezhad, A. Lajvardi, The effect of basin shape on the amount of sediment, Bibliography number: 4535528, (2017).

[14] A. Alighardashi, D. Goodarzi, Simulation of depth and wind effects on the hydraulic efficiency of sedimentation tanks, Water and Environment Journal, 34 (4) (2019) pp. 432-440.
https://doi.org/10.1111/wej.12478

[15] F. Bouisfi, A. Bouisfi, H. Ouarriche, M. E. Bouhali, M. Chaoui, Improving Removal Efficiency of Sedimentation Tanks Using Different Inlet and Outlet Position, FME Transactions, 47 (4) (2019) pp. 894-900.
https://doi.org/10.5937/fmet1904894B

[16] N. Patel, J. Ruparelia, J. Barve, Experimental and simulation study of rectangular and circular primary clarifier for wastewater treatment, Environmental Technology & Innovation, 23 (2021) pp.1-12.
https://doi.org/10.1016/j.eti.2021.101610

[17] R. Monk**,** J.F. Willis, Designing water treatment facilities. JounalAWWA, 79 (2) (1987) pp. 45-57**.**
https://doi.org/10.1002/j.1551-8833.1987.tb02798.x

[18] A. L. Stamou, E. W. Adams, W. Rodi, Numerical modeling of flow and settling in primary rectangular clarifiers, Journal of Hydraulic Research. 27 (1989) pp. 665-682.
https://doi.org/10.1080/00221688909499117

[19] C. W. Hirt, B. D. Nichols, Volume of Fluid (VOF) Method for the Dynamics of Free Boundaries. Journal of Computational Physics 39 (1) (1981) pp. 201-225.
https://doi.org/10.1016/0021-9991(81)90145-5

[20] Flow-3D Users Manuals, v 11.1. (2016).

[21] A. Ghaderi, M. Dasineh, F. Aristodemo, A. Ghahramanzadeh, Characteristics of free and submerged hydraulic jumps over different macroroughnesses, Journal of Hydro-informatics, 22 (6) (2020) pp. 1554-1572.
https://doi.org/10.2166/hydro.2020.298

[22] M. Ahmadi, A. Ghaderi, H. Mohammad Nezhad, A. Kuriqi, S. D. Francesco, Numerical Investigation of Hydraulics in a Vertical Slot Fishway with Upgraded Configurations, Water, 13 (19) (2021) pp. 1-23.
https://doi.org/10.3390/w13192711

[23] S. Abbasi, S. Fatemi, A. Ghaderi, S. D. Francesco, The Effect of Geometric Parameters of the Antivortex on a Triangular Labyrinth SideWeir, Water, 13 (1) (2020) pp. 2-25.
https://doi.org/10.3390/w13010014

[24] Flow-3D, Help, V.11.2, Flow Science Inc.

ACTA TECHNICA JAURINENSIS
Vol. 15, No. 4, pp. 221-231, 2022
10.14513/actatechjaur.00679

A grading method for analyzing internal erosion processes of nano-silica improved sand

Mayao Cheng[1], Yang Zeng[2,*], Linsheng Chen[1], Hong Yang[1]

[1]School of Transportation and Civil Engineering &Architecture, Foshan University
Guangyun Road 33, Foshan City 528225, China
[2]School of Highway, Chang'an University
Middle Section of Nan'er Huan Road, Xi'an 710064, China
*e-mail:zy18882017394@163.com

Submitted: 24/09/2022 Accepted: 11/11/2022 Published online: 25/11/2022

Abstract: Internal erosion (IE) often occurs in poorly graded sand, one of the traditional treatments is reducing the permeability by grouting. In recent years, nano-silica becomes a choice of grouting materials as its low viscosity and good penetration capacity. According to present literature, the effect of decreasing loss mass during IE of fine sand and nano-silica improved sand (NIS) was rarely studied. One of the important reasons is that, mass loss during IE was previously focused on and was weighed after filtering the effluent by electronic balance. More accurate weighing method should be studied, because electronic balance can not accurately weigh fine particles. In this paper, nano-silica not only acted as the grouting material but also acted as the IE process signal. So, a new grading method was conducted to monitor the particle size distribution in the effluent and illustrate the process of IE. Erosion time and permeability were also recorded and analyzed as comparison. The experimental results showed that the grading method can monitor precisely the diameter of loss particles and the composition of the effluent, grading range of 1-1000 μm can be adopted to monitor the coagulation of silica gel particles (1-50 μm, average diameter 11±5 μm) and fine sand particles (50-100 μm, average diameter 65±7 μm), grading range of 1-1000 nm can be adopted to monitor the smaller coagulation of silica gel particles (concentrated in the range of 1-250 nm). Through grading method, the IE of NIS can be divided into three stages: Removal and release of unbonded nano-silica particles and unbonded fine particles; Movement and discharge of bonded particles; Expansion of pores and instability of the whole sample skeleton.

Keywords: Internal erosion; Nano-silica imrpoved sand; Particle size analysis; Grading method

I. INTRODUCTION

IE is one of the most common failures which threatens dams, tunnels and levees [1-5]. Soil nature and states determine the vulnerability of materials and govern the rate of IE. Under the IE influence, poorly graded soil will destabilize step by step with internal fine particles discharging through the network [6-7]. Three steps of IE were identified by Muresan et al [8].

- Firstly, internal defects gradually develop under hydraulic power (such as particle removal results in cumulative faults or displacements).
- Secondly, progress of suffusion, fine particles are ensnared to the pore of larger particles.
- Thirdly, extended pores or channels that are eroded backward.

Masi et al [9] monitored IE processes by time-lapse electrical resistivity tomography, and found that IE was a highly nonlinear dynamic process with time. Actually, some unimpressive evidences (like minor fissures, slides and depressions) were observed in the process of IE, while in rare cases, apparent geomorphic evidence could be found. For example, there are no abnormalities in dams at the beginning of IE, but the dams may collapse within a few hours with the lower toe of the levee begins to discharge like a spring. As the highly nonlinear dynamic process and hidden property of IE, it is important to monitor and analyze the process of IE using effective methods, and it is necessary to prevent the development of IE using appropriate control method.

Grouting were widely used to reduce the permeability of soil (grouting materials such as: cement, microfine cement, sodium silicate, organic polymers et al.). Indraratna et al [10] used lignosulfonate and cement as stabilizers, mixed with silt and compacted. Their results showed that the ability of erosion resistance of the improved silt was effectively improved. In order to improve the erosion resistance of slope soil, Pei et al [11] injected different concentrations of modified sodium carboxymethyl cellulose into the soil, their results showed that the water stability, shear strength and permeability coefficient of slope soil were effectively improved with the increase of concentration of modified sodium carboxymethyl cellulose. The best way to strengthen the soil of urban areas or historic sites was low-pressure grouting, the good penetration of sodium-silicate based material made it appropriate to low-pressure grouting, the viscosity and gelation time of sodium-silicate based material were controlled by adjusting the amount of catalyst [12]. These traditional materials are able to reduce permeability effectively and improve the strength of soil. But sometimes, the effect of controlling IE is not so ideal in certain conditions. For example, the particle diameters of cement-based slurries are mostly in the micron range, while the pores of fine/salty sands are in micron/nano scale, cement-based slurries can not effectively permeate through fine/salty sands. The outstanding rheological properties of sodium silicates and organic polymers, together with their low initials viscosities, facilitate permeation of soils as fine as silty sands. But sodium silicates have non-negligible shrinkage and insufficient durability, organic polymers are often toxic which will contaminate soil and groundwater.

Since the late 1980s, a new kind of materials called "nano-silica" has attracted attention in geotechnical Engineering, it has nano-scale particles, low viscosity, good penetration capacity, non-toxic and stable physicochemical properties [13-14]. Nano-silica was usually added in concrete to change the microstructure and bonding properties of cement slurry due to its high fineness and amorphous structure [15]. Nano-silica was also injected to improve the overall strength and stability of surrounding rock when the broken underground rock was excavated [16]. For prevent pollutant migration and saturated soil liquefaction, nano-silica could be grouted into ground to form anti-seepage barrier [17]. When nano-silica was used to improve loose sand, the literature shows that nano-silica could effectively reduce the pore volume of sand [18]. Nano-silica was mainly used as additive in concrete or injected with a small amount into soil/rock in the above applications. Nano-silica should be a good choice to prevent the internal erosion because of its nano-scale, especially for fine sand with micro pores inside. But as a new kind of grouting materials, nano-silica has not been used to prevent IE of fine sand yet, thus the anti-erodibility effect of nano-silica in fine sand has not been studied in the literature.

At present, research of IE process mainly focus on pure granular materials like silt, sand and gravel [19-22]. The understanding of IE phenomena relies mainly on laboratory experiments. Early experimental studies focused on the effect of particle size distribution in IE [23-24]. Then the spatial and temporal migration of fine particles were later recognized and qualitatively observed, and the axial displacement of tested soils under increased hydraulic gradient was measured quantitatively [25]. More recently, Fannin and Slanen [26], used mass loss, porosity change and permeability to distinct IE process. In previous IE tests, mass loss during IE was usually focused and was weighed by electronic balance, the effluent was collected, filtered and then dried to obtain the lost mass. If there were very fine particles in the effluent, it was hard to be collected and weighed. It is important to find an effective method to identify the process of IE when small particles in effluent is too hard to collect, filter and dry.

In view of the complexity of IE, the limitations of existing IE process monitoring techniques, and the micro/nano meter of NIS in IE, in this paper, a new grading method was conducted to study the IE process of NIS, and traditional drying method (weighing by electronic balance) was used for comparative analysis. In order to monitor the IE process of NIS, a series of the IE tests were performed on NIS. Two results can be obtained from the IE tests: Firstly, it might be possible to illustrate the development stages of IE of NIS by the grading method. Secondly, IE process of NIS was discrepancy with different curing time.

The structure of the paper is as follows. Section II introduces the related materials and method to realize the IE monitoring process of NIS. Section III gives results to measure the process of IE of NIS by the grading method. Finally, in Section IV, the conclusion is summarized.

II. MATERIALS AND METHODS

1. Characteristics and compact process of sand sample

In embankment dams and levees, the liner and core material are usually composed by poorly graded sand [27]. Internal erosion is very likely to happen when the fines content is between 15% and 30% [28-29]. In our IE test, standard graded sand was adopted by mixing particles of different sizes, the grain size ranged from 50 to 400 μm, the particle size distribution is as same as that of Fell. The standard sand was washed before use and dried in an oven (the temperature should be between 105 ℃ and 110 ℃).

The particle size distribution is shown in **Fig. 1**. The mixed sand was statically compacted in three layers, the final sand sample height was 100 mm. The physical properties of the sand samples are shown in **Table 1**. Internal erosion test was firstly conducted with sand sample before adding nano-silica, then water head and inflow velocity to achieve internal erosion were obtained.

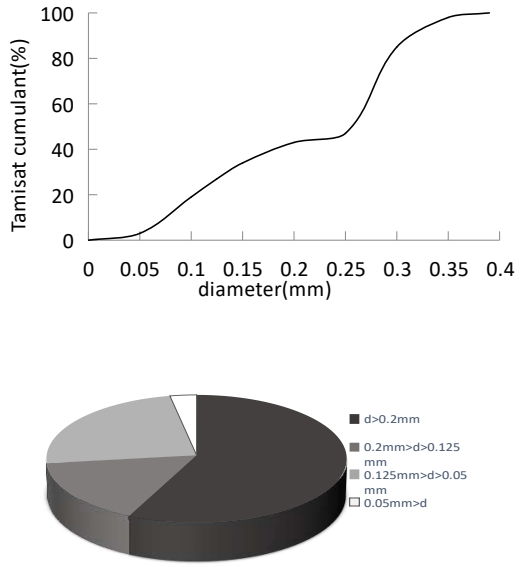

Figure 1. Grain size curve and proportion of particles of different sizes

Table 1. Mineral composition and physical properties of sand samples

Sand properties	The mixed sands
Density (g/cm^3)	1.60
Porosity	0.38

2. Modified nano-silica sol

Table 2. Basic physical properties of nano-silica sol and catalyst

Properties	Nano-silica	catalyst
Dynamic viscosity (mPa.s)	10	1
Density (kg/L)	1.1	1.07
pH	10	7
Concentration (% by weight)	SiO_2 15%	NaCl 10%

3. The sample preparation process

In our experiment, the amount volumetric of colloidal silica was set to 25% of the pore volume of sand column. Therefore, the sand and the nano-silica were mixed together instead of grouting. The mixture was statically compacted in three layers, the final sand column had a height of 100 mm and diameter of 50 mm. The porosity of sand columns after adding nano-silica was 0.29. The prepared columns were stored in the environment of 20 ℃ and 50% relative humidity for 2, 7 and 30 days. The NIS was designated as D2, D7 and D30 respectively. The initial permeabilities of D2, D7 and D30 were measured before IE test, which equalled 2.07×10^{-6} m/s; 2.17×10^{-6} m/s and 2.73×10^{-6} m/s, respectively.

4. Testing apparatus

The IE test equipment consisted of water supply reservoir, inflow pump, hydraulic transducer, effluent reservoir and particle sizing analyser (**Fig. 2**). The IE tests were conducted at constant inflow rate (50 mL/min) from the top. Hydraulic transducers were conducted at the top and bottom of column to monitor the change of water head. NIS's weight and mass loss, distribution of particles and water head were recorded with the erosion time. The measuring range of hydraulic transducer was from 50 KPa to 2000 KPa, and the measurement accuracy was 0.10%. The size particles in effluent (from 0.01 to 100 μm) were measured by particle sizing analyzer. To reduce experiment error, all NISs were saturated before the scour experiment and each test result was obtained by 3 repeated tests.

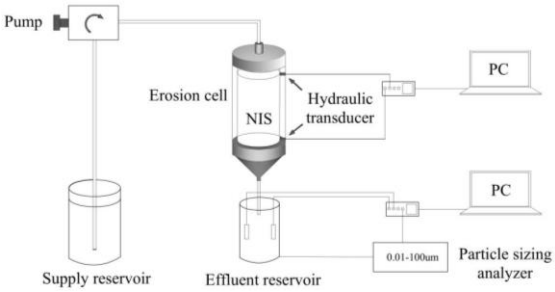

Figure 2. Experimental set-up for internal erosion tests.

5. Testing methods

To study the progress of IE, both the traditional drying method and the grading method were used at the same time. Test parameters include mass loss of NIS, porosity change and permeability change of NIS, size distribution of particles in the effluent.

A. Loss of NIS quality

The mass loss of NIS was obtained by the traditional drying method. The loss particles were filtered at different time points by sieves which can get particles larger than 100 μm. The loss particles were dried at 90 ℃ for 24 hours and weighed at a 0.1 g scale. The real-time weight of NIS was obtained by subtracting the total mass of lost particles from the original weight of the sample.

B. The porosity and permeability

The porosity is made up of two parts.

- when the particles remain stable without significant release, porosity is equal to the amount of inflow water.
- there exist newly formed pores and developing cracks. The quality of water in the void was determined by monitoring the NIS weights at a 0.1 g scale.

The increased volume of water in the pores can be obtained by dividing the mass of water by the density, So real-time porosity can be obtained. The permeability was obtained with Darcy law by measuring the velocity of inflow water and outflow water.

C. Size distribution of loss particles

To obtain the size distribution of particles in the effluent, particles larger than 100 μm were collected by sieves that placed above the lower sump. These particles (diameter larger than 100 μm) were mainly composed of highly insoluble (silica coated) sand particles. The size distribution of particles (diameter smaller than 100 μm) was obtained by the grading method. The grading method was conducted by two particle sizing systems (PSS). For diameter ranging from 1 to 100 μm, the diameter and the number of particles were measured by single-particle optical sensing equipment (AccuSizer™ 780 optical PSS). These particles were constituted by sand particles and coagulation of silica gel particles. For diameter ranging from 1 to 1000 nm, the diameter and the number of particles were measured by dynamic light scattering equipment (Nicomp™ 380 PSS) . This range of particles was silica gel particles.

III. RESULTS AND DISCUSSIONS

In advance of IE test of NIS, the IE test of unimproved sand was also conducted as comparison. Different inflow water rates were tested in the IE test of unimproved sand and NIS. For the unimproved sand: the IE developed very quickly under inflow rates of 10~40 mL/min; the granular structure of the unimproved sand sample was promptly destabilized under a inflow rate of 50 mL/min, the observed mechanism was not IE but quicksand, the cohesion between sand grains disappeared and notable amounts of sand were discharged within 1 minute. For the NIS, there was practically no IE phenomenon observed when the eroding fluid passing through at inflow rates of 10~40 mL/min. In order to obtain IE phenomenon of NIS, an constant inflow water rate of 50 mL/min was adopted.

1. The mass, the porosity and the permeability of NIS during IE

The mass of NIS and the mass of eroded particles (D2, D7 and D30) are exhibited in **Fig. 3(a)** and **Fig. 3(b)**. The results show three stages of IE.

- First stage of mass growth.
- second stage of plateau.
- last stage of mass loss.

Considering that the amount of particles flushed out in the early stage of the flushing experiment was large and changes rapidly, the measurement frequency at this stage was 5 min. In the subsequent long period of time, the internal structure of NIS was still relatively stable under the scouring of water flow, the lost particles were small in size and small in number, and the overall quality of NIS changes little. Therefore, this period of time was defined as the second stage in this paper, and the measurement frequency was 30 min.

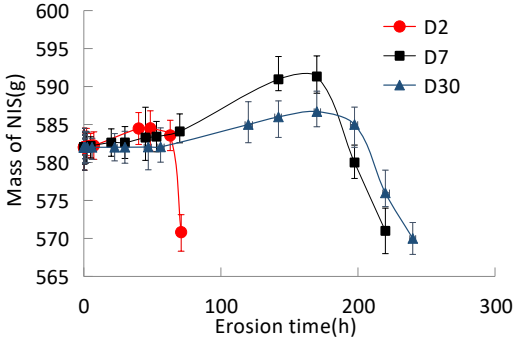

(a) the mass variation

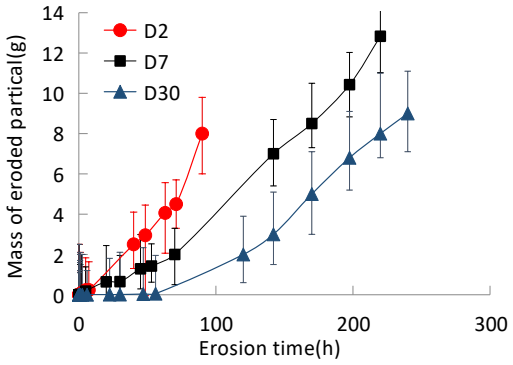

(b) mass of eroded particles

Figure 3. Evolutions of: (a) the mass variation, and (b) mass of eroded particles of D2, D7 and D30, respectively.

At the first stage, the mass of column grown with time {at t = (0~144)×10^3 s for D2, (0~511)×10^3 s for D7 and (0~510)×10^3 s for D30}. The mass intake rates for D2, D7 and D30 were 1.71×10^{-5} g.s^{-1}, 1.82×10^{-5} g.$s^{-1}$and 0.63×10^{-5} g.s^{-1} respectively. It can be deduced that in this stage, the unbonded nano-silica particles and unbonded fine particles began to move, more water flowed to the new holes and cracks.

At the second stage, the mass of column did not change with time {at t=(144~230)×10^3 s for D2, (511~612)×10^3 s for D7 and (510~711)×10^3 s for D30}. It supported existence of the second IE stage of unimproved sand when the mass was balanced: On the one hand, the continuing discharge of fine particles; On the other hand, increasing mass of inflow water occupied the holes and cracks in the

column. The continuing time of the second stage was 201×10^3 s for D30, which was much longer than that for D2 and D7 (86×10^3 s and 101×10^3 s, respectively). This phenomenon illustrated that, for D2, the improvement effect was not as good as D7 and D30. So, for the improved sand, the mass plateau of NIS meant no more mass loss, if this stage continued with time, no more IE happened, thus the nano-silica improvement was proved effective.

At the last stage, the curve of masses decayed quickly. The loss speed of mass was 97.05×10^{-5} g.s^{-1}, 80.65 ×10-5 g.s-1 and 66.26×10-7 g.s-1 for D2, D7 and D30 respectively. It was clear that the IE developed the most quickly for D2, and the IE developed the most slowly for D30. That was to say, nano-silica was more effective for 7 or 30 days' curing.

The porosity and the permeability of NIS in different scouring times are exhibited in Fig. 4(a) and Fig. 4(b).

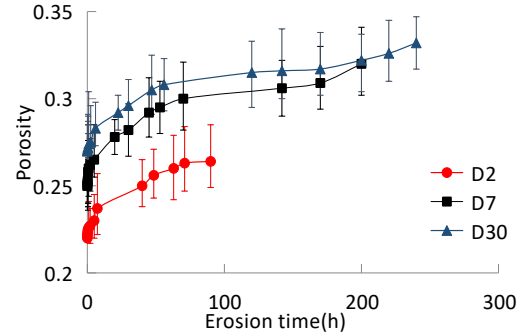

(a) pore volume

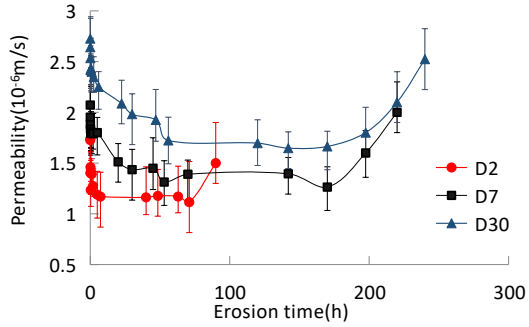

(b) intrinsic permeabilities

Figure 4. Evolutions of: (a) pore volume, and (b) intrinsic permeabilities of D2, D7 and D30, respectively.

In Fig. 4(a), the porosity during IE of D2, D7 and D30 are shown, we can summarize the following laws:

- At the first step, the porosity increased markedly, then the growth slowed down apparently, this law was consistent with the mass intake step which was obtained by mass analysis.
- At the second step, the curve tended to be flat, which showed that the sample structure was stable. The stabilization times lasted 52×10^3 s, 360×10^3 s and 410×10^3 s for D2, D7 and D30, respectively. The differences of stabilization time were more sensitive by analyzing porosity than mass change of columns.
- At the last step, the rate of growth suddenly accelerated, which indicated the increase of porosity due to particle's flushing. The period was corresponding to mass loss analysis {at (174.6-324) $\times10^3$ s for D2, (594–720) $\times10^3$ s for D7 and (612-864) $\times10^3$ s for D30}.

The failure stages of D7 and D30 were slower than that of sample D2. That was to say, nano-silica was more effective for 7 or 30 days' curing.

The permeability of sand was affected by the contraction geometry and the interconnections state between the pores. The result showed that the evolution of NIS permeability tended to decrease firstly, remained unchanged for a while and increased lastly. At the beginning of IE test, fine particles gradually moved under the action of inflow water, thus a temporary blockage of the pore channels happens in the bottom of NIS, which showed a rapid decrease of permeability. The similar law has been obtained in the references [30-32].

Then, after a period of stabilization, the permeability increased with the development of IE. The change law of permeability was mostly similar with that of mass and porosity, as all the factors were result from the three steps of IE development. But the permeability change was more sensitive in the first step due to the influence of blockage of fine particles in the bottom of sample. With the increased of curing time, the stabilizing time of second IE step increased. Compared with D2, the stabilizing time of D7 and D30 was longer, which indicated that the internal void's filling degree of D7 and D30 was higher.

2. The grading analysis of the effluent(1~1000 μm)

Fig. 5(a-c) shows the size composition (range of 1~1000 μm) of discharged particles during IE test. These particles were constituted by the coagulation of silical particles (1-50 μm, average diameter 11±5 μm) and fine sand particles (50-100 μm, average diameter 65±7 μm). The particle number of each size was precisely counted by AccuSizer™ 780 optical PSS, as a result, the particle number of each size was huge and was hard to show. The method of relative proportion method was adopted instead of showing numbers of particles.

Three factors are shown in each figure: erosion time, size of particles and occurrence probability. The numbers 0-10 above the chart represent the occurrence probability of the particles discharged during IE. The higher the number, the greater the

probability. On the other hand, it represents massive release of the particles with a certain size. The formula for the probability of occurrence is shown in (1).

$$p = 10\frac{d_n}{d_1} \quad (1)$$

n is the particle diameter (range of 1~1000 μm); d_n represents the total number of particles greater than or equal to the particle size; d_1 represents the total number of particles with a particle diameter greater than or equal to 1 μm, that is, the total number of particles

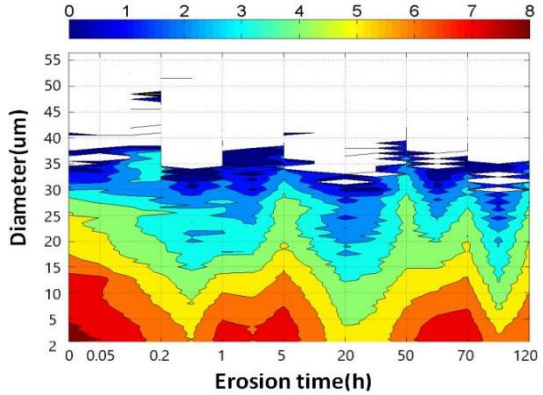

(a) D2

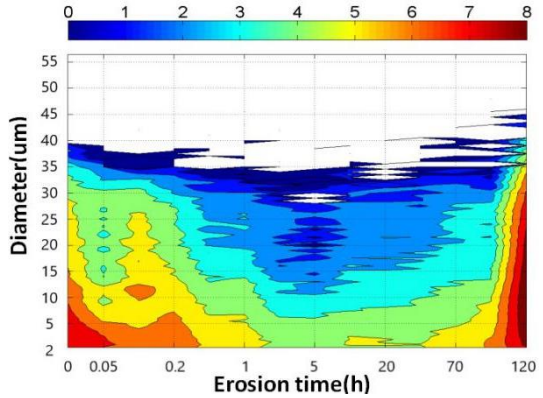

(b) D7

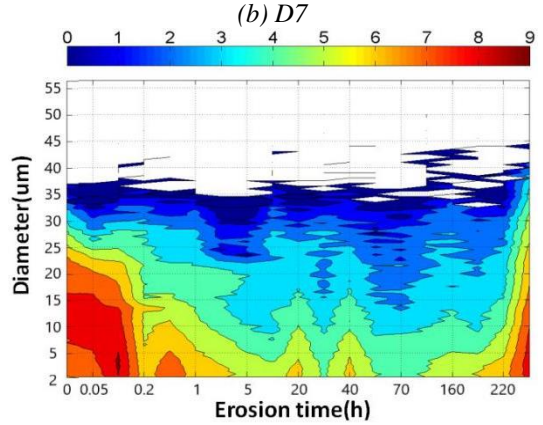

(c) D30

Figure 5. Contributions of micrometric particles (finest sand sample grains + eroded silica gel particles) to the instantaneous discharged mass of NIS for IE tests with (a) D2, (b) D7, and (c) D30, respectively.

Those tendencies were convex on both sides and concave in the middle. From quantitative perspective, those figures of D2, D7 and D30 showed that the discharges particle size was mostly concentrated in the range of 1-20, 1-15, 1-10 μm in first stage of IE (Lasting time about 1800 seconds). At the second stage, the corresponding discharged particles were concentrated in the range of 1-5 μm. At the last stage, the particles discharged rapidly, and the diameter of particle size was up to 80 μm. According to the results, those discharged particles demonstrated the continuous erosion. The weakening bonding effect of nano-silica leaded to the abundantly removal of fines and the subsequent instability of the coarse particles.

Those particles provided valuable information about IE dynamic evolution of NIS and the movement law of particles during IE. Particles discharged was mostly concentrated in the range of 1-20 μm in the first two steps of IE, which indicated that, the discharged particles were mostly the coagulation nano-silica which had less cohesive effect to sand particles and was easy to discharge. As indicated by previous results, most fine particles were initially fixed in closed pores or cavities, there were rare sand particles discharging in the first step of IE. Then, the swift released of particles bigger than 50 μm can be seen as signal of the discharge of fine sand particles the last stage. On the basis of those facts we can reach the following conclusion: After adding nano-silica, the development of IE was significantly delayed; The judgemental norm of IE step by proportion of fine sand particles should be raised; As well, more attention should be paid to the motoring the nano-silica discharged, and to study the cohesive effect of nano-silica; Nano-silica particles occupied a considerable part of 1-100 μm erosive particles either in the field of volume (70±8%, 79±8% and 73±15%, respectively) or mass (54±10%, 67±11% and 65±19%, respectively).

In Fig. 5(a-c), we can find that with the prolongation of curing time, the reinforcement effect of the samples gradually increased, and the erosion resistance time was prolonged. At the same flushing time point, the smaller the particle size and the smaller the number of flushed particles, which meant that the process of internal erosion was greatly slowed down and effectively suppressed with the prolongation of curing time.

3. The grading analysis of the effluent(1~1000 nm)

Fig. 6(a-c) shows the size composition (range of 1~1000 nm) of discharged particles during IE test. Monitoring the dynamic removal process of nano-silica particles was of great significance to study the seepage failure process of NIS. As nano-silica was nano-scale material, the nano-scale equipment (Nicomp™ 380 PSS) was used in trials to measure

the particle size distribution in the effluent. The results were shown in Fig. 6(a-c) with the same analytical method as the grading method for the effluent (particles range from 1 to 1000 nm).

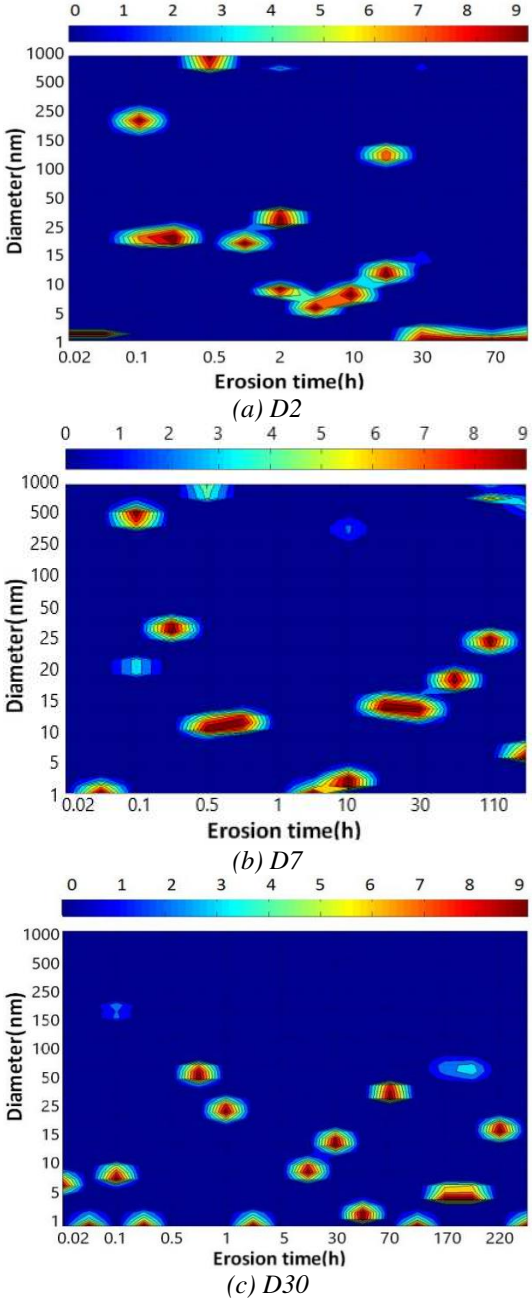

Figure 6. Contributions of nanometric particles (eroded silica gel particles) to the instantaneous discharged mass of NIS for IE tests with (a) D2, (b) D7, and (c) D30, respectively.

According to Kenney et al [33], when the size of the main channel of the filter structure is about 1/4 of the size of the particles that make up the filter structure in the pore network, fines can migrate in the channel. This means that the eroded silica gel particles (if the diameter is smaller than 11±5 μm) can pass through the narrow channel formed by the smallest particles of adjusted standard sand (average diameter of 65±7 μm). If the filling effect of nano-silica sol is good, the internal pore size can be limited or the diameter of the pore diameter can be reduced, the aim of enhancing structural stability and restraining erosion can be achieved. So, the lower concentration of silica particles primarily reflects the high stability to resist erosion (such as: D30).

At the beginning of IE test, the unstable nano-silica particles separated from NIS. The particle discharged was generally larger (diameter of 1-200 nm for D2 and D7 due to short curing time, while the particle discharged was smaller (diameter of 1-50 nm for D30 with sufficient curing time. At the middle of IE test, the plateau step started and stopped at different times: 0.16~1.10×105 s for D2, 0.22~3.82×105 s for D7 and 0.11~7.02×105 s for D30. At this stage, the loss particle sizes of D2, D7 and D30 were concentrated in the range of 1-10 nm,1-15 nm and 1-20 nm, respectively. The rigid skeleton formed by particles and binder can effectively support the imposed seepage stresses. This indicated that silica fragments were hardly got rid of sample under the effect of cementation. At the last step of IE test, small nano-silica particles increased and some large particles appeared in the effluent, the time of large particles appearing were (1.10-1.66)×105 s for D2, (3.82-4.14)×105 s for D7 and (7.02-8.46)×105 s for D30, respectively), which matched reasonably with the beginning of fine sand particles discharged, the phenomenon implied that instability of NIS can be gauged by observing the occurrence of silica particles.

4. The dynamics of particle transport within NIS

Fig. 7(a-c) shows the largest micrometric particles (LMP; left scale) and the smallest nanometric particles (SNP; right scale) in the effluent. The LMP represents those particles that successfully separate from NIS. The movement is blocked when the particle diameter is larger than the internal network channel, while the size of the eroded particles is smaller than the internal channel of NIS, these particles will flow through the pore network with the injected water. Therefore, the change of LMP can be regarded as the evolution process of the internal network channel size. The SNP describes the finest silica that can be mechanically dislodged from the binder by seepage. A rule can be assumed that SNP sizes should be proportional with seepage stresses: i.e. coarser silica colloids would be dislodged at higher shear forces.

From the LMP data, the LMP value was about twice the value obtained by Kenney's formula (~55 μm) at the beginning of IE test. The reason was that those superficial, unfiltered sand grains are discharged firstly. Later, {at t=(0.61~7.20, 1.19~3.60 and 0.29~1.19)×103 s for D2, D7 and D30, respectively}, The significant decreases of LMP signaled the further narrowing of the channel,

the minimal sizes of D2 rapidly tended to stabilize around 40~50 μm (70±1 and 60±3 μm for D7 and D30, respectively).

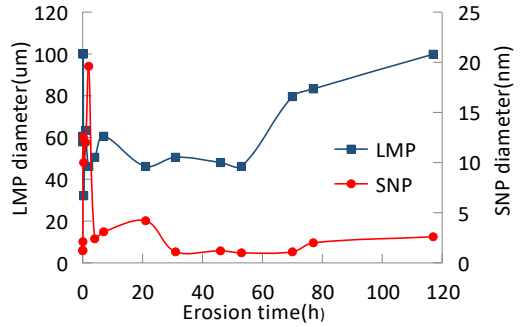

(a) D2

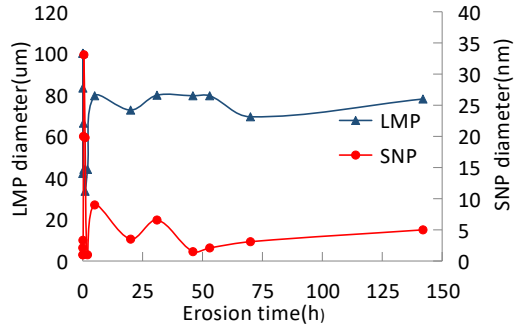

(b) D7

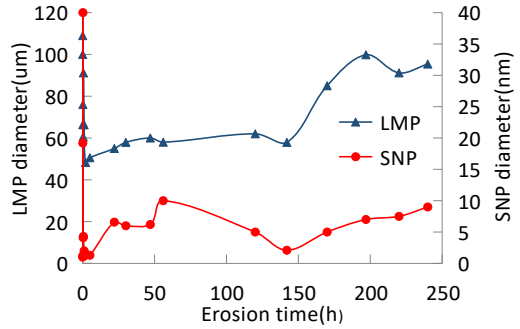

(c) D30

Figure 7. Diameters of largest micrometric particles in effluent (LMP; left scales, filled circles) and smallest nanometric particles in effluent(SNP; right scales, empty circles) for IE tests with (a) D2, (b) D7, and (c) D30, respectively

The diameter of the LMP was also maintained in a relatively stable range. SNP and LMP followed the similar laws. This phenomenon suggested that shear forces transfer some particles into the pore or network (such as unstable coarse silica fragments or sand grains) for partially blocking and filling the internal channels in early stage. Based on previous research and measured IE rates, the area of plateau not only described the low erodibility of NIS, but it also explained that the fine particles in motion (50~100 μm) were blocked by binder. At last, in the stage of mass loss, peaks of SNP matched with higher concentrations of grains (50~100 μm) {at t = (2.77~4.21)×106 s for D2, (6.10~7.63) ×106 s for D7 and (6.12~9.11)×106 s for D30}. By comparing the quality change curve obtained by the traditional drying method, the data of the grading method and has been verified, and it is simpler and more exact.

With the prolongation of curing time, the reinforcement effect of NIS gradually increased, and the erosion resistance time was prolonged. At the same scouring time point, the smaller the particle size and the smaller the number of flushed particles, which meant that the process of internal erosion was greatly slowed down and effectively suppressed with the prolongation of curing time

5. Data synthesis

The grading method was conducted and compared with the traditional drying method. The IE development law of NIS was summarized.

- At the first stage, mass growth was related to the filling of pores by inflow water and the flushing of movable unbonded nano-silica particles and unbonded fine sand particles. At this step, through the grading method, it was found that the particle size of the lost particles decreased markedly.
- At the second stage, the internal structure of the sample was stable, the IE developed very slowly, while the size of particle in the effluent kept in a low value.
- At the last stage, the mass loss revealed the dynamic release of particles and the gradual instability of the rigid skeleton. The increase of porosity and permeability showed that pores or capillary channels developed significantly, and the range of particle size in the effluent increased significantly.

IV. CONCLUSIONS

For soil with fine particles and small pores, grouting and monitoring the process of internal erosion is difficult. This research was planned and carried out with the purpose of filling the scientific gaps regarding the use of new method as replacement of the traditional drying method for monitoring IE of NIS. The laboratory research results of IE process of NIS were introduced. The grading method and the traditional drying method were compared and analyzed. The grading method can identify the process of IE of NIS by monitoring the distribution of particle size in the effluent with time. The process of IE of NIS can be divided into three stages:

- Removal and release of unbonded nano-silica particles and unbonded fine particles.
- Movement and discharge of bonded particles.

- Expansion of pores and instability of the whole sample skeleton.

Grading range of 1-1000 μm can be adopted to monitor the coagulation of silica gel particles (1-50 μm, average diameter 11±5 μm) and fine sand particles (50-100 μm, average diameter 65±7 μm). In the second stage, a large number of particles with 1-5 μm appeared, indicating that the internal structure of NIS began to be destroyed. In the third stage, when large particles with 50-100 μm appeared, NIS can no longer bear the damage of IE.

Grading range of 1-1000 nm can be adopted to monitor the smaller coagulation of silica gel particles (concentrated in the range of 1-250 nm). The range of particle size corresponding to the second stage is 1-20 nm. When the number of particles in this range rapidly decreased, it indicated that IE had entered the third stage and NIS was about to be destroyed..

With the extension of curing time, the impermeability of NIS improved, which can be judged by the appearance time of each particle size.

This study successfully demonstrate that the grading method is more accurate and simpler than traditional drying method for soil with fine particle and small pore size. So, for ensure the safety of the underground structure, it is necessary to monitor IE of NIS by the grading method in long time. We have to point out that only one graded sand sample is used in our research. the IE rule of NIS after 30 days of curing is also not considered. In the future research, we will gradually improve the grading method to test the improved soil with different grades and longer curing time.

REFERENCES

[1] M. Foster, R. Fell and M. Spannagle, The statistics of embankment dam failures and accidents. Canadian Geotechnical Journal 37 (5) (2000) pp. 1000-1024. https://doi.org/10.1139/t00-030

[2] M. Foster, R. Fell and M. Spannagle, Method for assessing the relative likelihood of failure of embankment dams by piping. Canadian Geotechnical Journal 37 (5) (2000) pp. 1025-1061. https://doi.org/10.1139/cgj-37-5-1025

[3] L. Caldeira, Internal Erosion in Dams: Studies and Rehabilitation. International Journal of Civil Engieering 17 (4) (2005) pp. 457-471. https://doi.org/10.1007/s40999-018-0329-5

[4] G. A. Fox and G. V. Wilson, The Role of Subsurface Flow in Hillslope and Stream Bank Erosion: A Review. Soil Science Society of America Journal 74 (6) (2010) pp. 717-733. https://doi.org/10.2136/sssaj2009.0319

[5] Correia et al, Experimental study on crack filling by upstream fills in dams. Géotechnique 64 (3) (2015) pp. 218-230. https://doi.org/10.1680/geot./14-P-198

[6] L. Ke and A. Takahashi, Strength reduction of cohesionless soil due to internal erosion induced by one-dimensional upward seepage flow. Soils & Foundations 52 (4) (2012) pp. 698-711. https://doi.org/10.1016/j.sandf.2012.07.010

[7] L. Ke and A. Takahashi, Triaxial Erosion Test for Evaluation of Mechanical Consequences of Internal Erosion. Geotechnical Testing Journal 37 (2) (2014). https://doi.org/10.1520/GTJ20130049

[8] B. Muresan, N. Saiyouri, A. Guefrech and P. Y. Hicher, Internal erosion of chemically reinforced granular materials: A granulometric approach. Journal of Hydrology 411 (3-4) (2011) pp.178-184. https://doi.org/10.1016/j.jhydrol.2011.09.009

[9] M. Masi, F. Ferdos, G. Losito, and L. Solari, Monitoring of internal erosion processes by time-lapse electrical resistivity tomography. Journal of Hydrology 589 (1) (2020) pp. 125340. https://doi.org/10.1016/j.jhydrol.2020.125340

ACKNOWLEDGMENTS

The publishing of this paper was supported by Regional Joint Fund Project of Basic and Applied Basic Research in Guangdong Province (2019A1515111100); Research project on characteristic innovation of university teachers from Foshan Education Bureau （2021XJZZ10）; Young Creative Talents Program in Guangdong Province (2019KQNCX170); Engineering technology research and Development Center for intelligent marine and terrestrial geotechnical material in Foshan and Basic and Applied Basic Research in Guangdong Province (2020A1515111137).

AUTHOR CONTRIBUTIONS

M. Cheng: Experiment, Investigation, Software, Data curation, Formal analysis, Writing-review & editing.

Y. Zeng: Experiment, Data analysis, Formal analysis, Writing-review & editing.

L. Chen: Experiment, Data analysis.

H. Yang: Investigation, Experiment.

DISCLOSURE STATEMENT

The authors declare that they have no known competing financial interests or personal relationships that could have appeared to influence the work reported in this paper.

[10] B. Indraratna, T. Muttuvel, H. Khabbaz and R. Armstrong, Predicting the erosion rate of chemically treated soil using a process simulation apparatus for internal crack erosion. Journal of Geotechnical and Geoenvironmental Engineering 134 (6) (2008) pp. 837-844. https://doi.org/10.1061/(ASCE)1090-0241(2008)134:6(837)

[11] X. J. Pei, Q. W. Yang, Q. Xu, X. C. Zhang, Y. Huang, Research on glue reinforcement mechanism and scouring resistant properties of soil slopes by modified carboxymethyl cellulose. Chinese Journal of Rock Mechanics and Engineering 35 (11) (2016) pp. 2316-2327. https://doi:10.13722/j.cnki.jrme.2015.1060

[12] G. Spagnoli, A review of soil improvement with non-conventional grouts. International Journal of Geotechnical Engineering 1 (15) (2018) pp. 273-287. https://doi.org/10.1080/19386362.2018.1484603

[13] S. M. A. Zomorodian, S. Moghispoor, B. C. O'Kelly, S. S. Babaei, Improving internal erosion resistance of silty sand using additives. Dams and Reservoirs 30 (1) (2020) pp. 29-41. https://doi.org/10.1680/jdare.20.00007

[14] P. M. Gallagher and Y. Lin, Colloidal Silica Transport through Liquefiable Porous Media. Journal of Geotechnical and Geoenvironmental Engineering 135 (11) (2009) pp. 1702-1712. https://doi.org/10.1061/(ASCE)GT.1943-5606.0000123

[15] S. Francisco Santos, J. de Anchieta Rodrigues, G. H. Denzin Tonoli, A. E. F. de Souza Almeida, H. Savastano Jr, Effect of colloidal silica on the mechanical properties of fiber-cement reinforced with cellulosic fibers, Journal of Materials Science. 49 (2014) 7497-7506, https://doi.org/10.1007/s10853-014-8455-1

[16] K. G. Holter, H. O. Hognestad, Modern pre-injection in underground construction with rapid-setting microcements and colloidal silica – Applications in conventional and TBM-tunnelling, Geomechanics and Tunnelling. 5(1) (2012) 49-56, https://doi.org/10.1002/geot.201200001

[17] B. Iranpour, A. Haddad, The influence of nano-materials on collapsible soil treatment. Engineering Geology. 205 (2016) 40-53, https://doi.org/10.1016/j.enggeo.2016.02.015.
T. C. Kenney and D. Lau, Internal stability of granular filters. Canadian Geotechnical Journal 22 (2) (1985) pp. 215-225. https://doi.org/10.1139/t85-029

[18] C. Todaro, Grouting of cohesionless soils by means of colloidal nanosilica. Case Studies in Construction Materials (15) (2021). https://doi.org/10.1016/j.cscm.2021.e00577

[19] L. M. Reddi, I. M. Lee, M. V. S. Bonala, Comparison of internal and surface erosion using flow pump tests on a sand-kaolinite mixture. Geotechnical Testing Journal 23 (1) (2000) pp.116-122. https://doi.org/10.1520/GTJ11129J

[20] F. Bendahmane, D. Marot and A. Alexis, Experimental Parametric Study of Suffusion and Backward Erosion. Journal of Geotechnical & Geoenvironmental Engineering 134 (1) (2008) pp. 57-67. https://doi.org/10.1061/(ASCE)1090-0241(2008)134:1(57)

[21] M. Ouyang and A. Takahashi, Influence of initial fines content on fabric of soils subjected to internal erosion. Canadian Geotechnical Journal 53 (2) (2016) pp. 299-313. https://doi.org/info:doi/10.1139/cgj-2014-0344

[22] M. Foster and R. Fell, Assessing Embankment Dam Filters That Do Not Satisfy Design Criteria. Journal of Geotechnical & Geoenvironmental Engineering 127 (5) (2001) pp. 398-407. https://doi.org/10.1061/(ASCE)1090-0241(2001)127:5(398)

[23] F. W. Chi and R. Fell, Assessing the Potential of Internal Instability and Suffusion in Embankment Dams and Their Foundations. Journal of Geotechnical & Geoenvironmental Engineering 134 (3) (2008) pp. 401-407. https://doi.org/10.1061/(ASCE)1090-0241(2008)134:3(401)

[24] R. Moffat, R. J. Fannin and S. J. Garner, Spatial and temporal progression of internal erosion in cohesionless soil. Canadian Geotechnical Journal 48 (3) (2011) pp. 399-412. https://doi.org/10.1139/T10-071

[25] R. J. Fannin and P. Slangen, On the distinct phenomena of suffusion and suffosion. Géotechnique Letters (4) (2014) pp. 289-294. https://doi.org/10.1680/geolett.14.00051

[26] D. Marot, F. Bendahmane, F. Rosquoet and A. Alexis, Internal flow effects on isotropic confined sand-clay mixtures. Soil Sediment Contam 18 (3) (2009) pp. 294-306. https://doi.org/10.1080/15320380902799524

[27] R. Fell, P. MacGregor, D. Stapledon and G. Bell, Geotechnical engineering of dams. (2005). https://doi.org/10.1201/NOE0415364409

[28] D. S. Chang and L. M. Zhang, Extended internal stability criteria for soils under seepage. Soils Found 53 (4) (2013) pp. 569-583. https://doi.org/10.1016/j.sandf.2013.06.008

[29] K. Boschi, C. G. Prisco and M. O. Ciantia, Micromechanical investigation of grouting in soil. International Journal of Solids and Structures (187) (2019) pp. 121-132. https://doi.org/10.1016/j.ijsolstr.2019.06.013

[30] Z. Hu, Y. D. Zhang and Z. X. Yang, Suffusion-induced deformation and microstructural change ofgranular soils: a coupled CFD-DEM study. Acta Geotechnica 14 (3) (2019) pp. 795-814. https://doi.org/10.1007/s11440-019-00789-8

[31] Oueidat, Mohamad, A. Benamar and A. Bennabi, Effect of Fine Particles and Soil Heterogeneity on the Initiation of Suffusion. Geotechnical and Geological Engineering 39 (3) (2021). https://doi.org/10.1007/s10706-020-01632-8

[32] T. C. Kenney, R. Chahal, E. Chiu, G. I. Ofoegbu, G. N. Omange, and C. A. Ume. Controlling constriction sizes of granular filters. Canadian Geotechnical Journal 22 (1) (1985) pp. 98-98. https://doi.org/10.1139/t85-005

ACTA TECHNICA JAURINENSIS
Vol. 15, No. 4, pp. 232-238, 2022
10.14513/actatechjaur.00677

The effect of coupling agent on the mechanical properties of injection molded polypropylene/wheat straw composites

László Lendvai[1,2*], Amar Patnaik[3]

[1]Polymer Institute, Slovak Academy of Science,
Dubravska cesta, 9, 845 41 Bratislava, 45, Slovakia
[2]Department of Materials Science and Engineering, Széchenyi István University,
Egyetem tér 1., Győr 9026, Hungary
[3]Department of Mechanical Engineering, Malaviya National Institute of Technology Jaipur
Jaipur 302017, India
*e-mail: lendvai.laszlo@sze.hu

Submitted: 22/08/2022 Accepted: 25/11/2022 Published online: 30/11/2022

Abstract: The objective of this work is to evaluate the effect of maleic anhydride-grafted polypropylene (MAPP) as coupling agent in polypropylene (PP)-based composites filled with ground wheat straw (WS) particles. The WS and the MAPP content in the composites was 10 wt% and 2 wt%, respectively. The samples were fabricated through melt compounding using a twin-screw extruder and then formed into dumbbell-shaped specimens by injection molding. The mechanical properties of neat PP and the composites with and without coupling were evaluated based on tensile and flexural tests and dynamic mechanical analyses (DMA). The experimental results showed that incorporating WS into the PP reduces its tensile strength by ~3 MPa, while improving its Young's modulus by 0.14 GPa. The addition of MAPP compensated for the loss in tensile strength without affecting the modulus. Similar observations were made during the flexural tests as well, in which case, however, there was no loss revealed in the strength in the presence of WS due to the different types of load. The results of DMA analyses indicated an improved stiffness of WS-containing samples throughout the whole analyzed temperature range of 20-120 °C as a consequence of reduced chain mobility of PP caused by the stiff straw particles.

Keywords: polypropylene; composites; natural fibers; wheat straw; mechanical properties; injection molding

I. INTRODUCTION

Natural fiber-reinforced thermoplastics gained more and more interest throughout the last several years, mostly due to the increasingly strict environmental regulations and the demand for sustainable lightweight plastic products. As a result, the importance of composites containing vegetable-based additives grew significantly in many fields, including the packaging, building, and automotive industries [1-3].

Polypropylene (PP) is one of the most versatile commodity plastics, which is produced in large quantities. The foremost reason for PP attracting major industrial and scientific interest lately is the wide variety of properties that can be achieved by combining it with other polymers or different fillers [4, 5]. Such property-tailoring actions enable the fabrication of highly ductile PP-based polymer blends with superior toughness [6, 7], and reinforced composites for engineering applications [8] at the same time. Within the last several years, numerous scientific studies were devoted to the development of PP-based polymer composites filled with various natural fibers [9, 10].

A specific type of natural fiber-filled composites is the group where polymers are filled with fibers generated as by-products during agricultural and forest industrial activities [11-14]. The foremost advantages of such lignocellulosic fillers are their low density, non-abrasive characteristics, high stiffness, low cost and, most importantly that they come from an annually renewable resource, while also being biodegradable [15]. Wheat straw (WS) is such an agricultural residue that is generated in vast amounts during the harvesting of wheat worldwide. In many countries, agricultural residues such as WS are still being gotten rid of through open-air burning,

which poses a considerable threat to the air quality, and through that to public health as well [16].

Incorporating lignocellulosic residues, like wheat straw into polymeric matrices, comes with a major challenge of forming a proper interfacial adhesion between the two components, else, the straw particles might act as stress concentration sites, leading to an early failure, when the polymer is exposed to a critical mechanical load. The generally poor interfacial compatibility between PP and natural fillers is due to the large polarity difference [17].

To date, a number of techniques have been introduced in order to improve the surface compatibility between plastics and natural fillers to produce high-performance composites. These techniques include physical methods (steam cooking, plasma treatment, etc.) and chemical pretreatments (alkaline treatment, mercerization, acetylation, etc.) as well [18]. Another potential way to promote the adhesive forces acting between the natural fibers and the polymer matrix is the use of coupling agents. For inert polymers, such as PP, the most commonly used coupling agents are the acid-modified versions of the base polymer [19]. In the case of PP it is the maleic anhydride-grafted polypropylene (MAPP), which is often used for natural filler-containing composites based on PP matrix. MAPP has been successfully used to improve the mechanical properties of polymer composites with PP matrix and various natural fillers, including jute [20], bamboo [21], wood [22], coconut fiber [23], banana fiber [24], and hemp [25].

In this present study, the effect of MAPP has been evaluated regarding the mechanical properties of ground WS particles-filled PP composites, where the test objects were prepared through injection molding. The quasi-static mechanical properties of the prepared samples were investigated by means of tensile and flexural tests, and the temperature-dependent mechanical properties were measured through dynamic mechanical analysis.

II. MATERIALS AND METHODS

1. Materials

An injection molding grade PP (Tipplen H145F), kindly supplied by MOL Petrochemicals (Tiszaújváros, Hungary) was used as a polymer matrix (density = 0.9 g/cm^3; MFI = 29 g/10 mins – measured at 2.16 kg and 230 °C). Chopped WS fibers were provided by Miko-Stroh (Borota, Hungary). The wheat straw fibers were washed in distilled water, dried, and sieved prior to blending them with PP. Particles were collected from sieves between 125 µm and 250 µm gaps. Optical microscopic image of the wheat straw can be seen in **Fig. 1.** The bulk density of wheat straw particles is

Figure 1. *Optical microscopic image of the wheat straw used as a natural filler*

reported to be in a wide range, mostly depending on its porosity, which, on the other hand, is greatly affected by the particle size [26]. The density of the straw particles used in this current study were determined to be ~1.49 g/cm^3. The coupling agent was a maleic anhydride-grafted polypropylene (MAPP) under the brand Polybond 3002, which was obtained from Crompton Company (Middlebury, Connecticut, USA). It has an MFI of 7 g/10 mins at 230 °C and 2.16 kg load.

2. Sample preparation

All the components (PP pellets, MAPP, and WS particles) were dried in a Faithful drying chamber (Model WGLL-125BE, Huanghua, Cangzhou, China) at 80 °C for 6 hours prior to the processing. Melt compounding was performed on a Labtech twin-screw extruder (Model LTE 20-44, Samut Prakarn, Thailand). Melt compounding was performed with a barrel temperature profile of 160, 160, 165, 165, 170, 170, 170, 175, 175, 180, and 180 °C from feeder to die. The rotational speed of the screws was 40 rpm, while starve feeding was applied by gradually pouring premixed dry batches of 30 g into the extruder. The extruded strings were cooled down in a water tank and pelletized subsequently. The designations, the compositions and the density (determined according to Archimedes' principle) of the fabricated samples are listed in **Table 1**. The measured density values confirmed that the resulting ratios of the components

Table 1. *Designation and composition of the prepared composite samples and their density*

Desig-nation	*PP [wt%]*	*WS [wt%]*	*MAPP [wt%]*	*Density [g/cm^3]*
PP	100	-	-	0.90
PP_WS	90	10	-	0.93
PP_WS_C	88	10	2	0.93

equal the theoretical values with little to no porosity being present in the samples. The composite pellets were dried once more prior to further processing with the same parameters as before the melt compounding.

The prepared composites were formed into dumbbell-shaped specimens according to the standard ISO 3167 as per injection molding, which was performed using an Arburg Allrounder machine (Model 420C, Lossburg, Germany) with a screw diameter of 35 mm. The heating zones of the injection unit were set to 170, 180, 190, 200, and 210 °C from the feeder to the nozzle. The mold was tempered to 25 °C. The injection rate was 30 cm^3/sec, while the injection pressure was 1000 bar. A holding pressure profile of 750-650-250 bar was used for a total of 10 sec.

3. Characterization

The tensile and flexural mechanical properties of the PP/WS composites were determined using an Instron universal testing machine (Model 5582, Norwood, Massachusetts, USA). The tensile tests were performed according to the ISO 527 standard at a crosshead speed of 25 mm/min and with a gripped length of 100 mm. For the three-point bending tests the ISO 178 standard was followed, using rectangular specimens of 80 × 10 × 4 mm^3, and the span length was set to 64 mm.

Dynamic mechanical analyses (DMA) were carried out in order to analyze the temperature-dependent mechanical properties of the prepared samples. For this purpose, a TA Instruments DMA machine (Model Q800, New Castle, Delaware, USA) equipped with a dual cantilever grip was applied. A heating rate of 3 °C/min was used in the temperature range of 20-120 °C. The amplitude was set to 0.02% deformation, while the frequency was 1 Hz. The specimens were rectangular bars with a length of 55 mm and a cross-section of 10 × 4 mm^2.

III. Results and Discussion

1. Tensile mechanical properties

Typical tensile stress-strain curves of PP and its WS-filled composites are displayed in **Fig. 2.**, while the corresponding tensile properties (i.e. tensile strength, Young's modulus, and elongation) are collected in **Table 2**. The incorporation of 10 wt% of WS resulted in a slight loss of strength, compared to neat PP (27.6 MPa vs. 30.7 MPa), which is ascribed to the poor stress transfer efficiency between the PP matrix and the straw particles. This can be attributed to the difference in polarity between the components. While straw fibers are greatly hydrophilic, PP is a hydrophobic material. The addition of 2 wt% MAPP as a coupling agent successfully compensated part of the loss in strength caused by the straw fibers, which

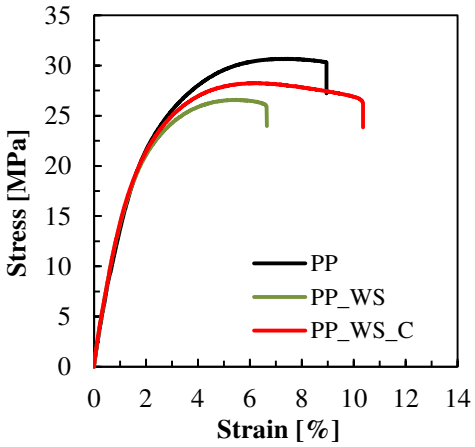

Figure 2. *Typical stress-strain curves recorded during the tensile tests*

refers to its efficiency in improving the interfacial interactions between PP and the straw. This is in good agreement with scientific studies dealing with similar topics [27, 28].

It is clear that the Young's modulus of unfilled PP (1.61 GPa) was greatly enhanced by the addition of WS. A relative improvement of 8-9% was achieved for both PP_WS (1.75 GPa) and PP_WS_C (1.74 GPa) samples. The explanation for the composites with and without coupling agent exhibiting very similar modulus values can be explained by the fact, that the quality of adhesion does not play a crucial role at low levels of mechanical loads, in which stage the Young's modulus is determined. Similar findings were also reported in the literature dealing with PP/WS composites containing straw particles of various size and concentration [29]. Interestingly, Ashori et al. [30] found increasing modulus values in the presence of 2 wt% maleated PP coupling agent,

Table 2. *Tensile mechanical properties of PP and its WS-filled composites with and without coupling agent*

	PP	***PP_WS***	***PP_WS_C***
Tensile strength [MPa]	30.7 ± 0.3	27.6 ± 0.6	28.1 ± 0.1
Young's modulus [GPa]	1.61 ± 0.02	1.75 ± 0.03	1.74 ± 0.03
Elongation at yield [%]	7.37 ± 0.16	5.47 ± 0.03	6.12 ± 0.14
Elongation at break [%]	8.99 ± 1.21	6.79 ± 0.69	9.46 ± 1.10

which indicates that the characteristics (i.e. molecular weight) of the given MAPP might also influence the resulting stiffness of the PP/WS composites.

Considering the elongation at break of the samples, the neat PP broke rather early (8.99%) even before showing a necking phenomenon, which is, however, in most cases not typical for this polymer. The lack of necking can be ascribed to the low molecular weight of the specific PP grade used in this study and the relatively high crosshead speed during the tensile tests. Introducing the WS resulted in a drop in deformability, reducing the elongation at break to 6.79%. In this regard, the sample containing MAPP as a compatibilizer proved to be superior (9.46%) compared to the previous ones. This supports the assumption that the maleated PP coupling agent promotes the interfacial adhesion between the components, making the composites able to endure higher levels of deformation.

2. Flexural mechanical properties

Comparative stress-strain curves recorded during the 3-point bending tests are shown in **Fig. 3**., while **Table 3** summarizes the flexural mechanical property values of the prepared samples. Even though the ISO 178 standard does not consider the flexural strength of polymeric materials when the deflection exceeds the conventional limit, currently, both the flexural stress at conventional deflection and the flexural strength values have been collected to describe the mechanical behavior of the fabricated samples.

The flexural modulus of both WS-containing samples outperformed the unfilled PP (1.66 GPa), as a consequence of stiff straw particles being present in the polymer. Similarly to the tensile tests' results, there is little to no difference agent in the modulus values determined through the 3-point bending tests, regardless of the presence of the coupling. Both the

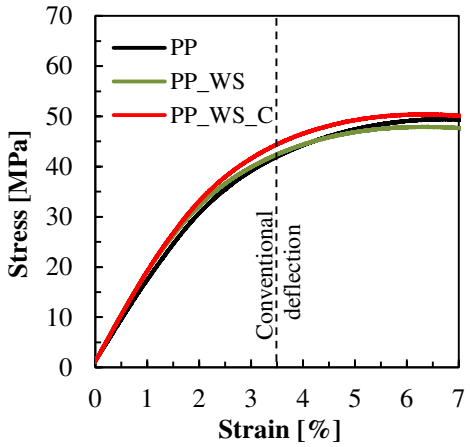

Figure 3. *Typical stress-strain curves recorded during the flexural tests*

Table 3. *Flexural mechanical properties of PP and its WS-filled composites with and without coupling agent*

	PP	***PP_WS***	***PP_WS_C***
Flex. stress at conv.defl. [MPa]	41.8 ± 0.5	42.9 ± 0.5	43.9 ± 0.3
Flexural strength [MPa]	49.8 ± 0.4	48.7 ± 0.6	50.5 ± 0.2
Flexural modulus [GPa]	1.66 ± 0.02	1.89 ± 0.03	1.89 ± 0.03

PP_WS and the PP_WS_C composites showed a flexural modulus of 1.89 GPa, which refers to the lack of significance of the coupling agent considering the stiffness.

Apparently, the flexural stress at conventional deflection values of both WS-containing composites were higher than that of unfilled PP (41.8 MPa). This is, however, partly due to the higher stiffness. Higher stiffness increases the initial slope of the flexural stress-strain curves, making them cross the limit of conventional deflection at higher stress values unless failure occurs earlier than that. On the other hand, the flexural strength of PP_WS (48.7 MPa) was lower than that of neat PP (49.8 MPa) due to the poor stress transfer between the polymer and the filler. Interestingly, the addition of MAPP, in this case, did not only compensate for the loss in strength, but the PP_WS_C composite (50.5 MPa) outperformed even the neat PP in terms of flexural strength. This means that under the bending type of load, the straw particles actually acted as reinforcement in PP, which was enabled by the successful stress transfer in the presence of maleated polypropylene compatibilizer. Similar results, namely enhanced flexural strength values of PP/WS composites in the presence of MAPP were reported by Panthapulakkal et al. [27] as well.

3. Dynamic mechanical properties

Comparison plots of the storage modulus (*E'*) and loss factor (*tan δ*) as a function of temperature were obtained through the DMA measurements. The corresponding curves are presented in **Fig. 4**. Evidently, the storage modulus of all samples decreases as a function of temperature, which can be attributed to the softening of PP. Compared to neat PP, the WS-containing samples exhibited a different DMA behavior. The *E'* curves of WS-filled composites shifted to higher modulus values due to the greater stiffness of straw particles compared to the polymer matrix. The plots of the PP/WS composites with and without MAPP are mostly

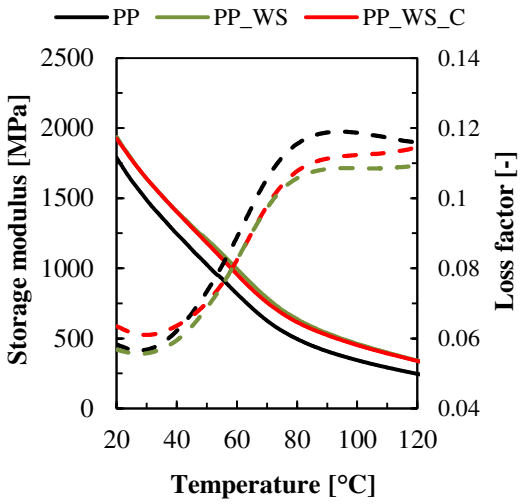

Figure 4. *Storage modulus (continuous curves) and loss factor (dashed curves) of PP and its WS-filled composites with and without coupling agent*

overlapping, indicating the fact that the presence of the coupling agent did barely alter the storage modulus of the system in the investigated temperature range. At room temperature (~25 °C), the storage modulus of the samples PP, PP_WS, and PP_WS_C was 1626 MPa, 1779 MPa, and 1775 MPa, respectively. This is in good agreement with both the tensile and flexural tests' results. The reason for the coupling agent-containing curve being slightly lower is explained in the literature by the formation of a thin and irregular polymer layer around the filler particles, which promotes plastic deformation. Similar trends were observed in the literature by Pan et al. [31] for compatibilized PP/WS composites, where the authors prepared the samples through compression molding.

Regarding the loss factor (*tan δ*), which is the ratio of loss modulus to storage modulus, the addition of WS particles resulted in lower values in the entire temperature range, referring to a decreased molecular mobility of PP, which is in good accord with the findings registered throughout the tensile and the flexural tests, namely an increased stiffness. Considering the rather stiff nature of the straw particles it seems reasonable that their presence restricted the motion of the polymer chain molecules.

IV. Conclusions

In this research, the effect of maleated polypropylene as a coupling agent was investigated, considering the quasi-static and dynamic mechanical properties of PP/WS composites. The samples were prepared through extrusion followed by injection molding, while the properties were analyzed by means of tensile tests, flexural tests, and DMA measurements. According to the results, the incorporation of WS into the PP matrix leads to enhanced stiffness, however, at cost of deteriorating strength and deformability due to the limited interfacial adhesion between the components. Adding the MAPP coupling agent to the composite system promotes the chemical interactions, thereby improving the strength of PP/WS composites. In the case of tensile tests, the presence of MAPP compensated part of the loss in strength caused by WS, while in the case of flexural tests the strength of the compatibilized samples even exceeded that of neat PPs. The dynamic mechanical analysis revealed that the stiffness enhancement caused by WS is present throughout the entire analyzed temperature range and is not affected by MAPP, while the damping factor of the composites decreased due to the stiff straw particles limiting the molecular mobility of PP.

Acknowledgment

The project was supported by the Prime Minister's Office (Hungary) through the National Talent Programme, project Nr. NTP-NFTÖ-21-B. L. Lendvai is grateful for the National Scholarship Programme of the Slovak Republic. The authors are grateful for MOL Petrochemicals Co. Ltd. for providing the polypropylene used in this study. The authors are grateful for Mikó Stroh Borotai-Laska Ltd. for providing the chopped wheat straw. The authors thank Dr. M. Omastova for her support regarding the dynamic mechanical analysis.

AUTHOR CONTRIBUTIONS

L. Lendvai: Conceptualization, Methodology, Experiments, Investigation, Theoretical analysis, Funding acquisition, Writing – Original draft preparation

A. Patnaik: Investigation, Theoretical analysis, Writing – Review and editing

Disclosure Statement

The authors declare that they have no known competing financial interests or personal relationships that could have appeared to influence the work reported in this paper.

ORCID

L. Lendvai http://orcid.org/0000-0003-3670-327X

A. Patnaik http://orcid.org/0000-0001-9506-782X

REFERENCES

[1] O. Akampumuza, P. M. Wambua, A. Ahmed, W. Li, X.-H. Qin, Review of the applications of biocomposites in the automotive industry, Polymer Composites 38 (11) (2017) pp. 2553–2569. https://doi.org/10.1002/pc.23847

[2] M. S. Huda, L. T. Drzal, D. Ray, A. K. Mohanty, M. Mishra,, Chapter 7, in: K. L. Pickering (Ed.), Properties and Performance of Natural-Fibre Composites, Woodhead Publishing, Sawston, 2008.

[3] S. Tejyan, N. K. Baliyan, V. K. Patel, A. Patnaik, T. Singh, Polymer green composites reinforced with natural fibers: A comparative study. Materials Today: Proceedings 44 (6) (2021) pp. 4767-4769. https://doi.org/10.1016/j.matpr.2020.10.971

[4] J. Karger-Kocsis, Polypropylene Structure, Blends and Composites, Chapman and Hall, London, 1995. https://doi.org/10.1007/978-94-011-0523-1

[5] J. Karger-Kocsis, T. Bárány, Polypropylene Handbook: Morphology, Blends and Composites, Springer International Publishing, Cham, 2019. https://doi.org/10.1007/978-3-030-12903-3

[6] L. Lendvai, A novel preparation method of polypropylene/natural rubber blends with improved toughness, Polymer International 70 (3) (2021) pp. 298-307. https://doi.org/10.1002/pi.6133

[7] I. P. Mahendra, B. Wirjosentono, Tamrin, H. Ismail, J. A. Mendez, V. Causin, The influence of maleic anhydride-grafted polymers as compatibilizer on the properties of polypropylene and cyclic natural rubber blends, Journal of Polymer Research 26 (2019) 215. https://doi.org/10.1007/s10965-019-1878-2

[8] L. Lendvai, Water-Assisted Production of Polypropylene/Boehmite Composites, Periodica Polytechica Mechanical Engineering 64 (2) (2020) pp. 128-135. https://doi.org/10.3311/PPme.13981

[9] S. Panthapulakkal, M. Sain, Injection Molded Wheat Straw and Corn Stem Filled Polypropylene Composites, Journal of Polymers and the Environment 14 (2006) pp. 265-272. https://doi.org/10.1007/s10924-006-0021-8

[10] H. Hargitai, I. Rácz, R. D. Anandjiwala, Development of HEMP Fiber Reinforced Polypropylene Composites, Journal of Thermoplastic Composite Materials 21 (2) (2008) pp. 165-174. https://doi.org/10.1177/0892705707083949

[11] T. Väisänen, A. Haapala, R. Lappalainen, L. Tomppo, Utilization of agricultural and forest industry waste and residues in natural fiber-polymer composites: A review, Waste Management 54 (2016) pp. 62-73. https://doi.org/10.1016/j.wasman.2016.04.037

[12] G. Dogossy, T. Czigány, Modeling and investigation of the reinforcing effect of maize hull in PE matrix composites, Polymers for Advanced Technologies 17 (9-10) (2006) pp. 825-829. https://doi.org/10.1002/pat.748

[13] T. Singh, S. Tejyan, A. Patnaik, V. Singh, I. Zsoldos, G. Fekete, Fabrication of waste bagasse fiber-reinforced epoxy composites: Study of physical, mechanical, and erosion properties, Polymer Composites 40 (9) (2019) pp. 3777-3786. https://doi.org/10.1002/pc.25239

[14] A. Gupta, A. Joshi, S. Tejyan, B. Gangil, T. Singh, Comparative study of mechanical properties of orange peel filled epoxy composites joined by a mechanical fastener, Materials Today: Proceedings 44 (6) (2021) pp. 4671-4676. https://doi.org/10.1016/j.matpr.2020.11.020

[15] M. Zabihzadeh, F. Dastoorian, G. Ebrahimi, Effect of MAPE on Mechanical and Morphological Properties of Wheat Straw/HDPE Injection Molded Composites, Journal of Reinforced Plastics and Composites 29 (1) (2008) pp. 123-131. https://doi.org/10.1177/0731684408096426

[16] M. Duque-Acevedo, L. J. Belmonte-Ureña, F. J. Cortés-García, F. Camacho-Ferre, Agricultural waste: Review of the evolution, approaches and perspectives on alternative uses, Global Ecology and Conservation 22 (2020) e00902. https://doi.org/10.1016/j.gecco.2020.e00902

[17] S. A. Paul, K. Joseph, G. D. G. Mathew, L. A. Pothen, S. Thomas, Influence of polarity parameters on the mechanical properties of composites from polypropylene fiber and short banana fiber, Composites Part A: Applied Science and Manufacturing 41 (10) (2010) pp. 1380-1387. https://doi.org/10.1016/j.compositesa.2010.04.015

[18] M. Chougan, S. H. Ghaffar, M. J. Al-Kheetan, M. Gecevicius, Wheat straw pre-treatments using eco-friendly strategies for enhancing the tensile properties of bio-based polylactic acid composites, Industrial Crops and Products 155 (2020) 112836. https://doi.org/10.1016/j.indcrop.2020.112836

[19] R. Fatoni, L. Simon, A. Elkamel, A. Almansoori, Wheat straw fibre size effects on the mechanical properties of polypropylene

composites, The Canadian Journal of Chemical Engineering 92 (10) (2014) pp. 1700-1708. https://doi.org/10.1002/cjce.22032

[20] S. Mohanty, S. K. Nayak, S. K. Verma, S. S. Tripathy, Effect of MAPP as a Coupling Agent on the Performance of Jute–PP Composites, Journal of Reinforced Plastics and Composites 23 (6) (2004) pp. 625-637. https://doi.org/10.1177/0731684404032868

[21] X. Chen, Q. Guo, Y. Mi, Bamboo fiber-reinforced polypropylene composites: A study of the mechanical properties, Journal of Applied Polymer Science 69 (1998) pp. 1891-1899. https://doi.org/10.1002/(SICI)1097-4628(19980906)69:10<1891::AID-APP1>3.0.CO;2-9

[22] L. Zhu, J. Cao, Y. Wang, R. Liu, G. Zhao, Effect of MAPP on interfacial compatibility of wood flour/polypropylene composite evaluated with dielectric approach, Polymer Composites 35 (3) (2014) pp. 489-494. https://doi.org/10.1002/pc.22686

[23] M. Sabri, A. Mukhtar, K. Shahril, A. S. Rohana, H. Salmah, Effect of Compatibilizer on Mechanical Properties and Water Absorption Behaviour of Coconut Fiber Filled Polypropylene Composite, Advanced Materials Research 795 (2013) pp. 313-317. https://doi.org/10.4028/www.scientific.net/AMR.795.313

[24] N. Amir, K. A. Z. Abidin, F. B. M. Shiri, Effects of Fibre Configuration on Mechanical Properties of Banana Fibre/PP/MAPP Natural Fibre Reinforced Polymer Composite, Procedia Engineering 184 (2017) pp. 573-580. https://doi.org/10.1016/j.proeng.2017.04.140

[25] T. Sullins, S. Pillay, A. Komus, H. Ning, Hemp fiber reinforced polypropylene composites: The effects of material treatments, Composites Part B: Engineering 114 (2017) pp. 15-22. https://doi.org/10.1016/j.compositesb.2017.02.001

[26] Y. Zhang, A. E. Ghali, B. Li, Physical Properties of Wheat Straw Varieties Cultivated Under Different Climatic and Soil Conditions in Three Continents, American Journal of Engineering and Applied Sciences 5 (2) (2012) pp. 98-106.

[27] S. Panthapulakkal, M. Sain, Injection Molded Wheat Straw and Corn Stem Filled Polypropylene Composites, Journal of Polymers and the Environment 14 (2006) pp. 265-272. https://dx.doi.org/10.1007/s10924-006-0021-8

[28] D. Pakuszta, M. Jedryczka, M. Binkiewicz, Mechanical properties of polypropylene composites filled with the straw of oilseed rape infested by the fungal pathogen *Sclerotinia sclerotiorum*, Journal of Composite Materials 47 (12) (2012) pp. 1461-1470. https://dx.doi.org/10.1177/0021998312448498

[29] S. A. Hashemi, M. Esfandeh, J. Mohammadi, Mechanical, Thermal and Rheological Properties of Polypropylene/ Wheat Straw Composites and Study of the Effect of Nanoclay on Their Mechanical Properties, Polymers and Polymer Composites 18 (2) (2010) pp. 67-73. https://dx.doi.org/10.1177/096739111001800202

[30] A. Ashori, A. Nourbakhsh, Mechanical Behavior of Agro-Residue-Reinforced Polypropylene Composites, Journal of Applied Polymer Science 11 (5) (2009) pp. 2616-2620. https://doi.org/10.1002/app.29345

[31] M. Pan, S. Y. Zhang, D. Zhou, Preparation and Properties of Wheat Straw Fiber-polypropylene Composites. Part II. Investigation of Surface Treatments on the Thermo-mechanical and Rheological Properties of the Composites, Journal of Composite Materials 44 (9) (2009) pp. 1061-1073. https://doi.org/10.1177/0021998309349549